

RESEARCH ARTICLE

MOLECULAR BIOLOGY

RNA editing restricts hyperactive ciliary kinases

Dongdong Li^{1,2,3,4}, Yufan Liu^{1,2,3,4}, Peishan Yi^{1,2,3,4}, Zhiwen Zhu^{1,2,3,4}, Wei Li⁵, Qiangfeng Cliff Zhang^{1,2,6,7}, Jin Billy Li⁸, Guangshuo Ou^{1,2,3,4,*}

Protein kinase activity must be precisely regulated, but how a cell governs hyperactive kinases remains unclear. In this study, we generated a constitutively active mitogen-activated protein kinase DYF-5 (DYF-5CA) in *Caenorhabditis elegans* that disrupted sensory cilia. Genetic suppressor screens identified that mutations of ADR-2, an RNA adenosine deaminase, rescued ciliary phenotypes of *dyf-5CA*. We found that *dyf-5CA* animals abnormally transcribed antisense RNAs that pair with *dyf-5CA* messenger RNA (mRNA) to form double-stranded RNA, recruiting ADR-2 to edit the region ectopically. RNA editing impaired *dyf-5CA* mRNA splicing, and the resultant intron retentions blocked DYF-5CA protein translation and activated nonsense-mediated *dyf-5CA* mRNA decay. The kinase RNA editing requires kinase hyperactivity. The similar RNA editing-dependent feedback regulation restricted the other ciliary kinases NEKL-4/NEK10 and DYF-18/CCKR, which suggests a widespread mechanism that underlies kinase regulation.

Protein kinases mediate signal transduction and regulate fundamental cellular processes in eukaryotic cells. The catalytic activity of kinases must be stringently controlled, and its dysregulation leads to developmental defects, metabolic disorders, and cancer (1, 2). Although loss-of-function kinase mutations have been extensively studied, gain-of-function mutations are less understood. Kinase hyperactivities have been described in many disease conditions, such as the constitutively active BCR-ABL1 tyrosine kinase in chronic myelogenous leukemia and BRAF serine/threonine kinase in malignant melanomas (1). Potent kinase inhibitors treat cancer effectively; however, tumors inevitably develop drug resistance and circumvent kinase inhibition by activating alternative pathways that perpetuate cell proliferation (3). Therefore, it is crucial to understand how an organism regulates hyperactive kinases.

We studied male germ cell-associated kinase (Mak), an evolutionarily conserved mitogen-activated protein kinase (MAPK). Mak localizes at the ciliary tip to restrict cilia elongation (2, 4, 5). Cilia are microtubule-based organelles essential for cell motility and sensory signaling, and ciliary defects cause more than 35 ciliopathies (6). The loss of Mak orthologs

results in abnormally long cilia and leads to retinitis pigmentosa (2, 4, 5, 7, 8). By contrast, overexpression of mammalian Mak or *Caenorhabditis elegans* genomic DNA (gDNA) encoding the Mak ortholog DYF-5 inhibits ciliogenesis (2, 5), which indicates that an optimal Mak/DYF-5 activity is essential. The MAPK superfamily contains a canonical TxY motif in the activation T-loop, phosphorylation of the threonine (pThr) residue activates the kinase, and glutamate can be a phosphomimetic pThr (9, 10).

Results

A constitutively active DYF-5 kinase disrupted cilia

We first established that substitution of Thr¹⁶⁴ with glutamate (T164E) in the TxY motif of DYF-5 leads to constitutive kinase activation in vitro. DYF-5(T164E) phosphorylated an intraflagellar transport (IFT) protein IFT-74, whereas wild-type (WT) DYF-5 did not (fig. S1, A to D), demonstrating that the substitution produced a constitutively active DYF-5 kinase (hereafter DYF-5CA). We then generated a T164E *dyf-5CA* knock-in animal in *C. elegans* (Fig. 1A and fig. S2, A and B). The *dyf-5CA* mutant ($n > 200$) exhibited normal morphology, viability, and growth rates comparable with those of the WT N2 strain. However, 87% of *dyf-5CA* worms ($n = 150$) could not use their sensory cilia to uptake fluorescence dye 1,1'-dioctadecyl-3,3',3'-tetramethylindocarbocyanine perchlorate from the medium (Dyf) (Fig. 1B and fig. S2C), indicating an impaired ciliary function and integrity (11). To visualize IFT and cilia, we introduced a green fluorescence protein (GFP)-tagged IFT52/OSM-6 into *dyf-5CA*. In contrast to the bidirectional motility of OSM-6::GFP in WT cilia (12), no IFT was detectable from the distal

ciliary segments of *dyf-5CA* ($n > 20$ animals), in which the OSM-6::GFP fluorescence formed aggregates (Fig. 1, C and D, and fig. S3, A and C to E).

The *dyf-5CA* animals developed abnormally elongated cilia, resembling the long cilia defect in the *dyf-5(mn400)* null allele (Fig. 1, B and D, and fig. S3B) but opposite to the truncated cilia phenotype when *dyf-5* gDNA was overexpressed (2). None of the *dyf-5CA* heterozygotes showed ciliary defects ($n > 50$ examined heterozygotes), and expression of the *dyf-5* cDNA in ciliated neurons fully rescued ciliary phenotypes in *dyf-5CA* (Fig. 1, B and D), indicating that *dyf-5CA* is a recessive loss-of-function mutant. Expression of *dyf-5CA* cDNA did not disrupt cilia in WT but rescued ciliary defects in *dyf-5CA* mutants (Fig. 1B and fig. S2D). Thus, the DYF-5CA protein did not have a dominant-negative effect. The discrepancy between the in vitro kinase hyperactivity and the in vivo kinase-null phenotype suggests that a previously unrecognized mechanism may control DYF-5CA in a living organism.

RNA adenosine deaminase mutations rescued ciliary defects by DYF-5CA kinase

We performed a forward genetic suppressor screen for mutations that restore *dyf-5CA* cilia (fig. S4A) and isolated four suppressors, *cas506*, *cas517*, *cas518*, and *cas519*, which exhibited uptake of fluorescence dye like the WT ($n = 100$) (fig. S4, B and C). All four mutations were mapped to the deaminase domain of ADR-2, with *cas517* carrying a premature stop codon and the other three mutants carrying missense mutations (Fig. 1E and fig. S4, B and D). A deletion mutant of *adr-2(ok735)* that removes the entire double-stranded RNA (dsRNA) binding domain and most of the deaminase domain (Fig. 1E and fig. S4E) showed the same ciliary rescue effects on *dyf-5CA* mutant cilia (Fig. 1, B and D, and fig. S3B).

ADR-2 is an ortholog of human ADAR1 (adenosine deaminase acting on RNA B1, or ADAR2). It exhibits dsRNA adenosine deaminase activity, catalyzing the adenosine-to-inosine (A-to-I) RNA editing, which is interpreted by the ribosome as guanosine (13, 14). The *C. elegans* genome encodes two ADARs: ADR-1 is catalytically inactive, and ADR-2 is the only active RNA deaminase. The *adr-2* deletion completely abolishes A-to-I editing (15–17). Although ADR-1 regulates the activity of ADR-2 (15), the *adr-1* deletion did not recover *dyf-5CA* cilia (fig. S4C). By contrast, the *adr-2* deletion reduced the ciliary aggregates of OSM-6::GFP and improved IFT in both amphid and phasmid cilia of *dyf-5CA* animals, albeit at a slower speed (Fig. 1D and fig. S3, A and C to E). None of the *adr-2* mutant alleles displayed ciliary defects ($n > 100$, for each genotype) (Fig. 1B and fig. S4C). We used a ciliated neuron-specific promoter, *Pdyf-1*, to express *adr-2* cDNA in the

¹Tsinghua-Peking Center for Life Sciences, Tsinghua University, Beijing, China. ²Beijing Frontier Research Center for Biological Structure, Tsinghua University, Beijing, China. ³McGovern Institute for Brain Research, Tsinghua University, Beijing, China. ⁴School of Life Sciences and MOE Key Laboratory for Protein Science, Tsinghua University, Beijing, China. ⁵School of Medicine, Tsinghua University, Beijing, China. ⁶MOE Key Laboratory of Bioinformatics, School of Life Sciences, Tsinghua University, Beijing, China. ⁷Center for Synthetic and Systems Biology, Tsinghua University, Beijing, China. ⁸Department of Genetics, Stanford University School of Medicine, Stanford, CA, USA.
*Corresponding author. Email: guangshouou@tsinghua.edu.cn

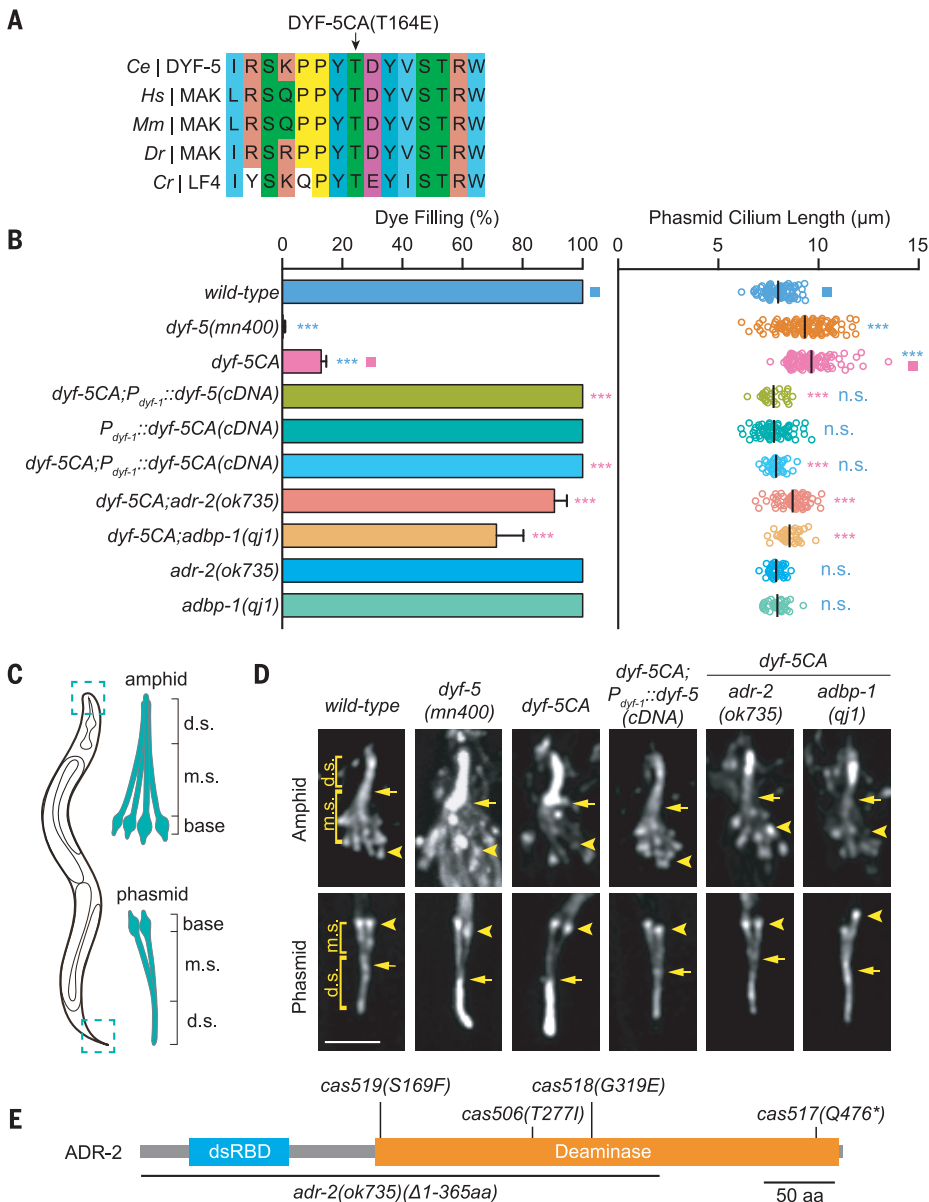


Fig. 1. ADR-2 mutations rescued ciliary defects in *dyf-5CA*. (A) Multi-sequence alignment of the *C. elegans* (Ce) DYF-5 kinase and its homologs in human (Hs), mouse (Mm), zebrafish (Dr), and *Chlamydomonas* (Cr). E, Glu; T, Thr. (B) Percentage of dye-filling positive animals in the indicated strains (mean ± SD) (left). N = 100 to 200. The cilium length of phasmid cilia (right, measured using the OSM-6::GFP fluorescence) is shown. N = 30 to 60. Statistical significance, compared with the control with a matching color code, is based on Student's *t* test; n.s., not significant, ****P* < 0.001. (C) Schematic of the amphid and phasmid cilia. Dashed boxes are enlarged on the right. d.s., distal ciliary segment; m.s., middle segment. (D) Cilia in WT and mutants. Arrowheads indicate the ciliary base and transition zone, and arrows indicate junctions between the middle and distal segments. Scale bar, 5 μm. (E) ADR-2 protein domains. Amino acid changes and the deletion in *adr-2* mutant alleles are indicated. dsRBD, dsRNA binding domain. F, Phe; G, Gly; I, Ile; Q, Gln; S, Ser. Scale bar, 50 amino acids (aa).

dyf-5CA; *adr-2* double mutant, which caused 75% of animals to develop the same ciliary defects that were observed in *dyf-5CA* animals (*n* = 300 transgenic animals) (fig. S4C), indicating that ADR-2 functions cell autonomously.

DYF-5CA caused aberrant RNA editing of the *dyf-5CA* pre-mRNA

We sought a mechanistic understanding between ADR-2 and DYF-5CA. An ADR-2::GFP reporter confirmed its nuclear localization (13) but did not reveal the ciliary localization of ADR-2 (fig. S5, A and B). Using GFP-affinity purification and mass spectrometry, we identified a known ADR-2 binding protein, ADBP-1, required for its deaminase activity (fig. S5C and data file S1) (18). The *adbp-1(qj1)* mutant recovered *dyf-5CA*'s ciliary defects (Fig. 1, B and D, and fig. S3, A to C), and GFP::ADBP-

1 localized within nuclei, but not cilia (fig. S5D), suggesting that ADR-2 and ADBP-1 do not directly function in cilia but regulate DYF-5CA by their nuclear actions. Because ADR-2 and ADBP-1 are involved in small interfering RNA- and microRNA-associated pathways (18–20), we introduced RNA interference (RNAi) mutants into *dyf-5CA* but did not observe rescue effects (fig. S5E), indicating that the function of *adr-2* or *adbp-1* is independent of the RNAi machinery.

To understand ADR-2-based RNA editing in *dyf-5CA*, we implemented a comparative RNA-sequencing (RNA-seq) screen on WT, *dyf-5CA*, *adr-2*, and *dyf-5CA*; *adr-2* animals by using an established computational pipeline (21). WT animals had a total of 18,097 A-to-I editing sites, but RNA editing events were almost undetectable in *adr-2* or *adbp-1* (Fig. 2A,

fig. S6A, and data file S2), which confirmed previous findings (15–18). In *dyf-5CA* animals, 12,871 sites that were edited in WT became unedited (Fig. 2A and data file S2). Because removing all the editing sites in the *dyf-5CA*; *adr-2* double mutant rescued *dyf-5CA*'s ciliary defects, we argue that these editing sites lost in *dyf-5CA* are not responsible for the phenotypes, although it is unclear why and how these sites were lost. The *dyf-5CA* animals unexpectedly acquired 1537 RNA editing sites, which were not detected in the WT and were lost in the *dyf-5CA*; *adr-2* (Fig. 2A and data file S2). Most of the identified RNA editing sites are located on chromosomes as clusters (17). We searched for the groups of ectopic editing sites and found that clustered sites were present in seven genes (fig. S6B and data file S2), including the *dyf-5CA* gene itself (Fig. 2B). The 269 editing

sites were distributed from the sixth exon to the seventh intron of *dyf-5CA* and occurred at frequencies of 10 to ~60% (Fig. 2C). By contrast, we did not detect any RNA editing sites in the *dyf-5* locus in other strains (Fig. 2B). Except for *dyf-5*, none of the other six genes were known to have ciliary functions.

We next investigated whether and to what extent the aberrant RNA editing clusters in *dyf-5CA* affect cilia. The sixth and seventh introns contain 130 editing sites, and the deletion of either intron or both in *dyf-5CA*

animals rescued ciliary defects (Fig. 2D and figs. S2A and S7, A and B). The double intron deletion removed all the ectopic editing clusters in *dyf-5* exons (Fig. 2B). To rule out the effects of intron deletion on pre-mRNA, we synthesized the sixth and seventh introns by placing a noneditable T at all detected A-to-I editing sites. Replacing introns with noneditable sites rescued the ciliary phenotypes in *dyf-5CA* (Fig. 2D and figs. S2A and S7, B and C). Although other aberrantly gained or lost RNA editing sites may have biological

functions under certain conditions, our data show that RNA editing sites in *dyf-5CA* are the primary cause for ciliary defects.

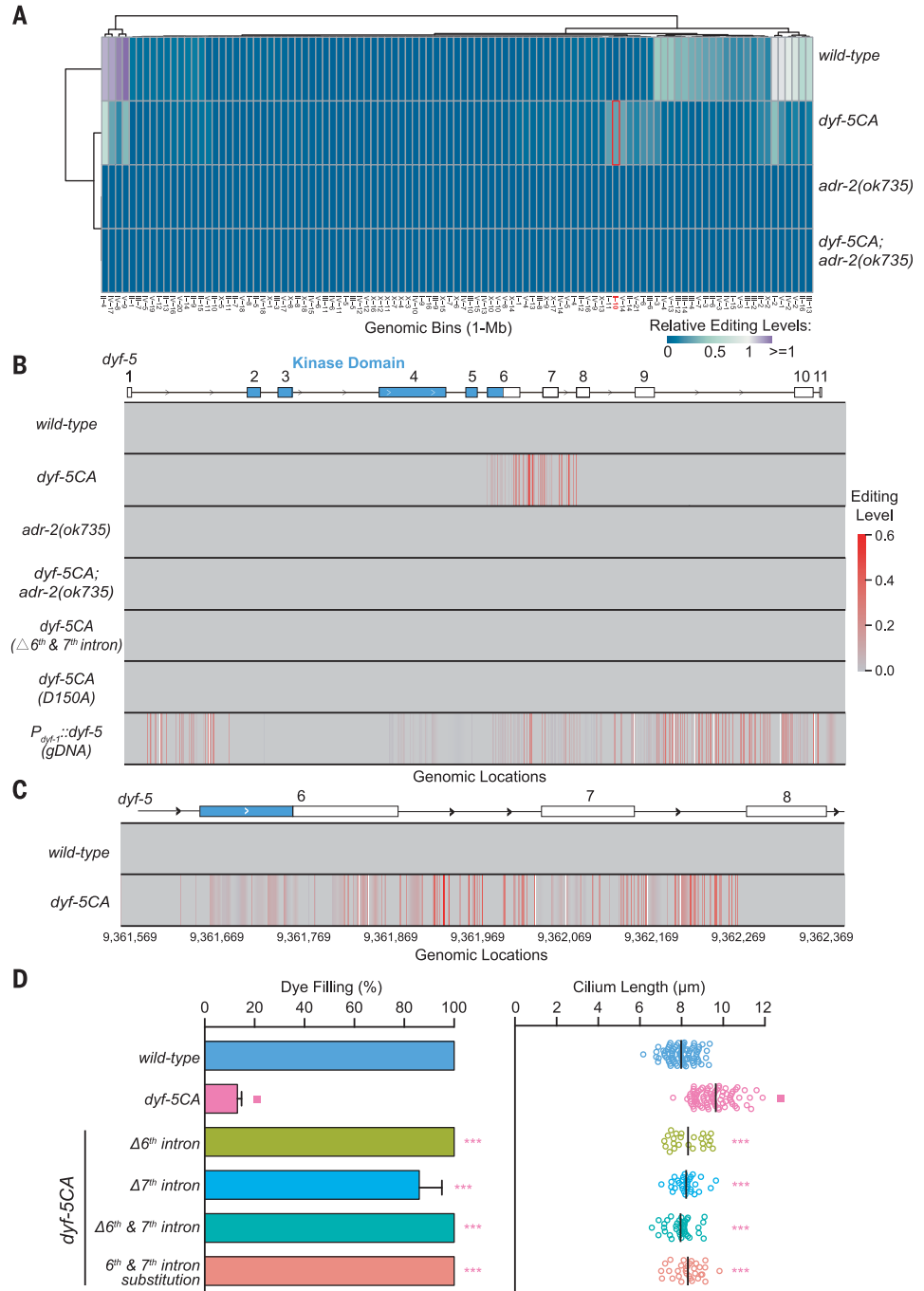
dyf-5CA animals generated antisense transcripts in *dyf-5*

Why does RNA editing occur specifically in this region? Because substrates of RNA editing enzymes are dsRNA (*13*), we examined whether long dsRNAs are formed intramolecularly at this locus but failed to identify any, which is consistent with lacking RNA editing at this

Fig. 2. ADR-2–dependent RNA editing clusters in *dyf-5CA*.

(A) Heatmap and dendrogram of hierarchical clustering of editing sites using editing ratios among WT and mutants in different genomic bins (1-Mb tile) from RNA-seq data. Relative editing levels were used in hierarchical clustering. Each row corresponds to a sample. Each column represents the relative editing ratio in a genomic bin. Experiments were repeated three times with the similar results.

The red box highlights the bin with the abnormally gained RNA editing sites of the *dyf-5* locus in *dyf-5CA*. (B) Representative RNA editing analysis at the *dyf-5* locus. Each row corresponds to a sample. Red lines represent RNA editing sites in the genomic locations of *dyf-5*, and the bar for editing level is shown on the right. Gene bodies are above; blue boxes show exons encoding the kinase domain. A, Ala; D, Asp. (C) Ectopic gain of RNA editing sites at the *dyf-5* locus in *dyf-5CA*. (D) Percentage of dye-filling (mean \pm SD) positive animals in the indicated strains, $n = 100$ to 200 (left). Cilium length, $n = 30$ to 60 (right), is shown.



locus in the WT. We then investigated whether an antisense RNA was generated to form dsRNA with the *dyf-5CA* transcript subject to ADR-2 editing. Our strand-specific RNA-seq detected abundant antisense transcripts in *dyf-5CA* animals, starting from the seventh intron to the fourth exon of *dyf-5CA* and aligning with the region where aberrant RNA editing occurred (Fig. 3, A and B). Next, we examined whether the eighth intron of *dyf-5*, which is immediately upstream of the antisense transcripts, regulates antisense transcription. Although *dyf-5* cDNA expression did

not cause ciliary abnormalities (Fig. 3C and figs. S2D and S8A), expression of *dyf-5* cDNA containing the sixth, seventh, and eighth introns, but not any individual intron, disrupted cilia (Fig. 3C). Conversely, *dyf-5* gDNA expression impaired cilia in an ADR-2-dependent manner (Fig. 3C and fig. S8A); however, expression of *dyf-5* gDNA that lacked the sixth, seventh, or eighth intron reduced the penetrance of ciliary defects (Fig. 3C). Consistently, *dyf-5* gDNA expression produced ectopic RNA editing clusters and antisense RNA transcription of *dyf-5*, which were not limited to the

regions in *dyf-5CA* animals but spread to additional introns and exons of *dyf-5* (Figs. 2B and 3A), generating more profound effects than *dyf-5CA*. Deleting the eighth intron reduced the ciliary defects of *dyf-5CA* animals (Fig. 3C and fig. S7B), which demonstrates its contribution to ciliary defects. The incomplete penetrance of the eighth intron deletion suggests that other genomic region(s) might be involved. This intron may serve as a cryptic promoter for antisense transcription, and future studies will need to identify the additional cis-regulatory elements and the corresponding trans factor(s).

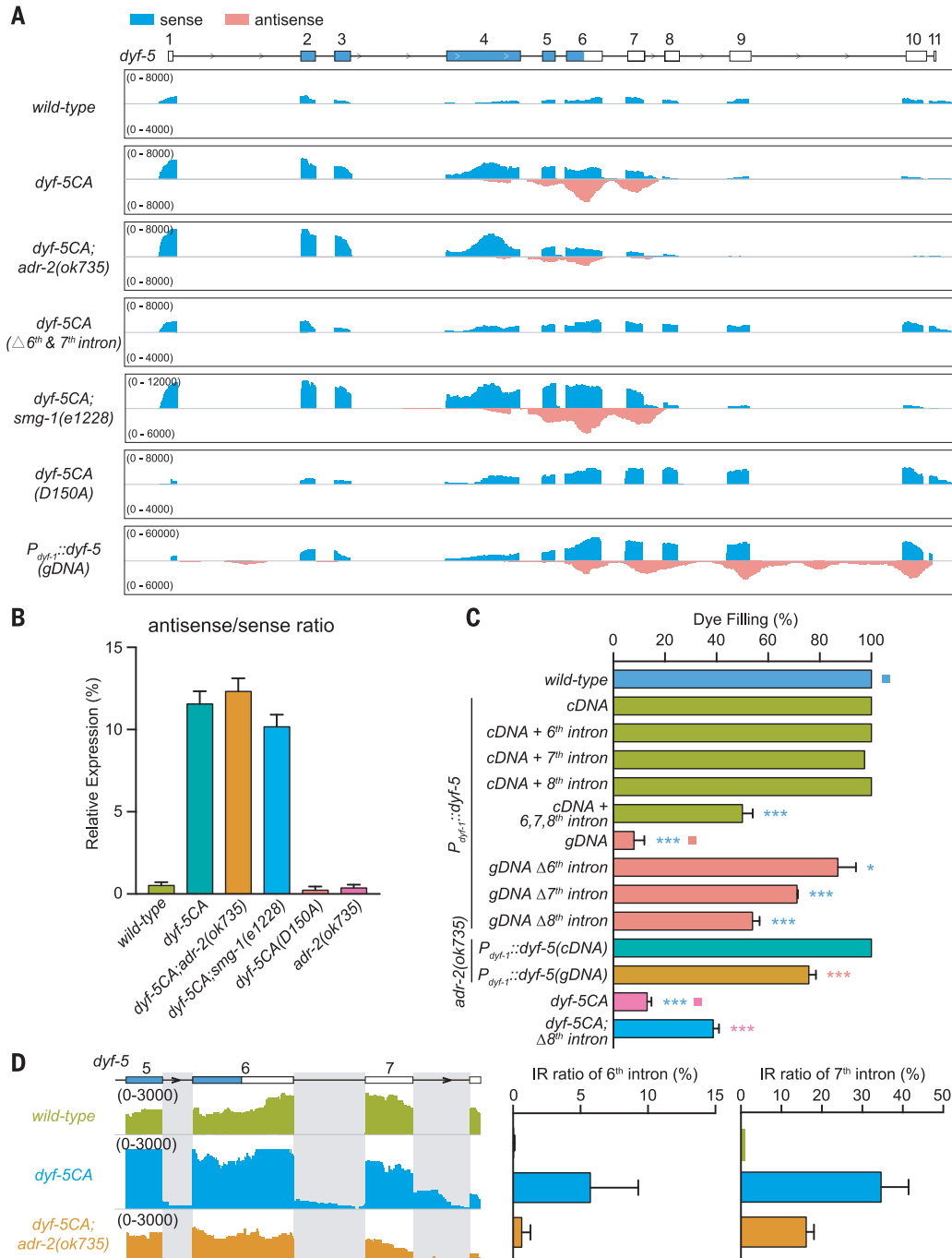


Fig. 3. Antisense RNA generation in *dyf-5CA*.

(A and B) RNA expression profiles at the *dyf-5* locus in different strains. Sense RNA (top) is in blue, and antisense RNA (bottom) is in pink. (B) Percentage of the normalized antisense/sense ratio in the indicated strains. Mean ± SEM. Experiments in (A) and (B) were performed three times with similar results. RNA-seq signals are shown in the labeled range. (C) Percentage of Dyf phenotypes in the indicated strains. $n = 100$ to 200, mean ± SD. (D) Distributions of normalized stranded RNA-seq reads for a portion of the *dyf-5* gene in (A) show IRs. Gray boxes show the location of retained introns. RNA-seq signals are shown in the labeled range (left). Data are from three independent experiments and show mean ± SEM (right).

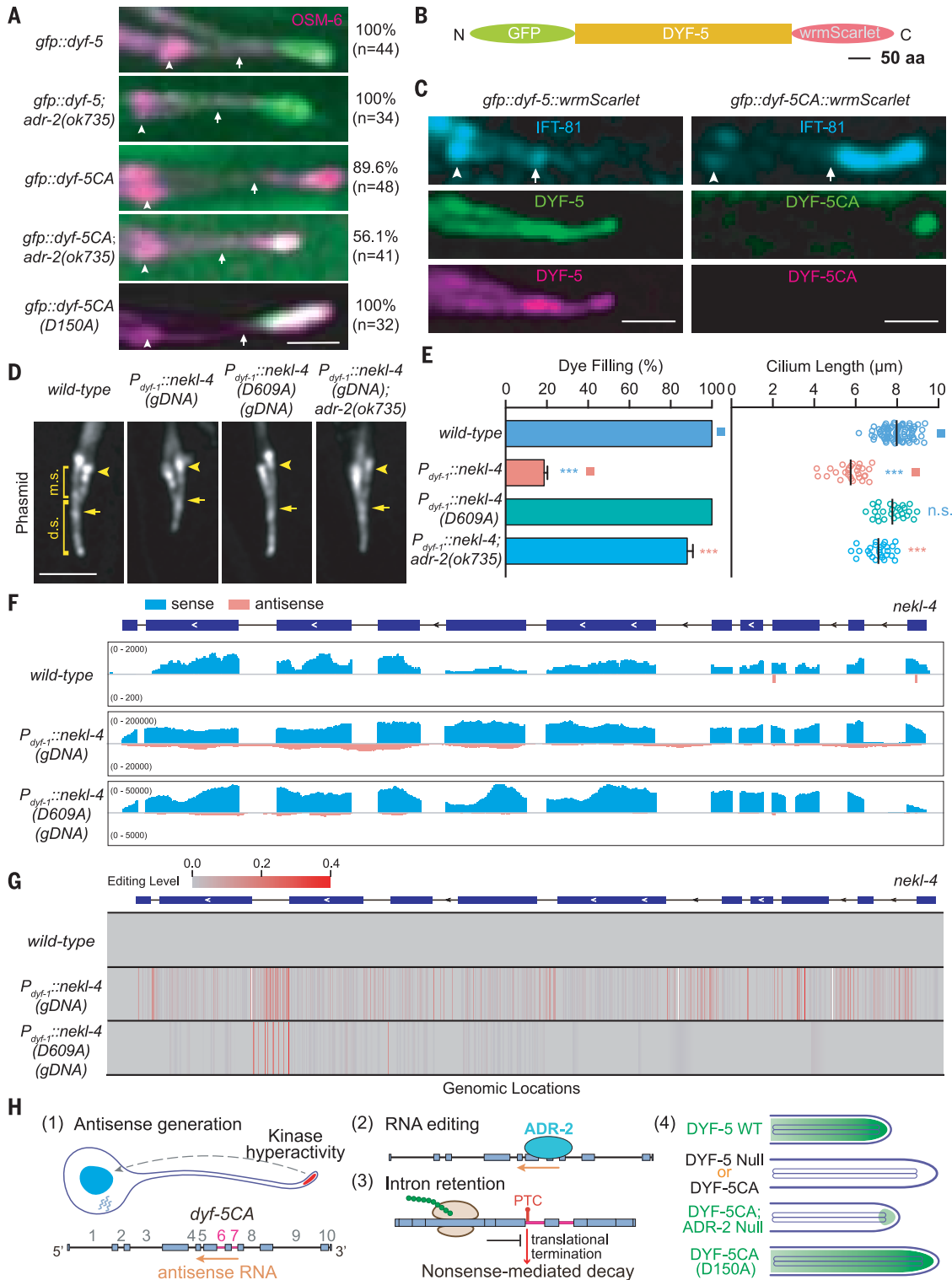


Fig. 4. DYF-5CA protein production and a working model. (A) Localization of GFP::DYF-5 or GFP::DYF-5CA with different genotypes. OSM-6::mCherry marks cilia. Percentages of DYF-5 localization patterns are indicated. (B) Schematic of *gfp::dyf-5::wrmScarlet* knock-in allele. Scale bar, 50 amino acids. (C) Localization of GFP::DYF-5::wrmScarlet (left) or GFP::DYF-5CA::wrmScarlet (right) in phasmid cilia. The blue fluorescence protein (BFP)-tagged IFT-81 labels cilia. Scale bars, (A) and (C), 2.5 μm. (D) Ciliary defects in the *nekl-4* gDNA overexpressed

animals. Scale bar, 5 μm. (E) Percentage of dye filling (mean ± SD)-positive animals, *n* = 100 to 200 (left). Cilium length, *n* = 20 to 40 (right). (F) Mapping profiles of sense and antisense RNA at *nekl-4* in the WT *nekl-4* (upper) or kinase-dead *nekl-4*(D609A) (lower) gDNA overexpression animals (sense reads, blue; antisense reads, pink). (G) RNA editing clusters at *nekl-4*. The bar for editing level is shown on the top. (H) Model summarizes how RNA editing restricts hyperactive ciliary kinases.

Impaired *dyf-5CA* mRNA splicing blocked DYF-5CA kinase translation

Whereas antisense transcripts resulted in promiscuous RNA editing in *dyf-5CA*, it is the RNA editing, but not the antisense transcripts, that caused ciliary defects because *dyf-5CA*; *adr-2* double mutants that retained antisense transcripts but lacked RNA editing restored their cilia (Fig. 3, A and B). Thus, we studied the molecular consequence that RNA editing conferred in *dyf-5CA*. The hyperediting of the sixth and the seventh exons changed 40.5% of the amino acids in this region. The sixth exon is located in the kinase domain, implying a possible down-regulation of kinase activity (fig. S7D). The sixth and the seventh introns in the *dyf-5CA* pre-mRNA were not sufficiently spliced out, causing intron retention (IR) (Fig. 3, A and D). Using IRFinder (22), we found that the sixth and seventh IR ratios are 5.7 and 34.6% in *dyf-5CA*, respectively (Fig. 3D). By contrast, IR ratios were reduced to 0.6 and 16% in the *dyf-5CA*; *adr-2* double mutant, indicating that RNA editing of the intron sequence may promote IR. The incomplete elimination of IR in *dyf-5CA*; *adr-2* double mutants suggests that other mechanisms may be involved. For example, RNA editing is known to occur cotranscriptionally in nascent RNAs (23), and the ectopic antisense RNA transcripts can form dsRNA to prevent the spliceosome from accessing the *dyf-5CA* pre-mRNA.

To examine kinase production, we fused GFP to DYF-5 at its N terminus in WT or *dyf-5CA* animals. DYF-5 localized in the WT or *adr-2* mutant cilia (100%, $n > 30$ animals) (Fig. 4A and fig. S8B); however, GFP fluorescence was barely detected from 89.6% of *gfp::dyf-5CA* animals (Fig. 4A and fig. S8C). In *gfp::dyf-5CA*; *adr-2* double mutants, the GFP::DYF-5CA signal increased, albeit at a lower level than the WT (Fig. 4A), indicating that a small amount of hyperactive kinase restored cilia. To further evaluate whether the loss of GFP::DYF-5CA resulted from translation blockade, we fused a red fluorescent protein gene (*wrmScarlet*, the Scarlet protein with worm codon optimization) to the C terminus of GFP::DYF-5 or GFP::DYF-5CA (Fig. 4B). The green and red fluorescence colocalized in all the *gfp::dyf-5::wrmScarlet* cilia ($n = 60$ animals) (Fig. 4C); however, only the faint green but no red fluorescence was visible from all the examined *gfp::dyf-5CA::wrmScarlet* animals ($n = 43$) (Fig. 4C), which implies premature translation termination. Furthermore, the GFP-tagged DYF-5 kinase domain (11 to 291 amino acids) was localized in the cell body and dendrite but not in cilia, whereas the C terminus of DYF-5 (292 to 489 amino acids) entered cilia (fig. S8, D to F), indicating that its C terminus targeted the kinase domain to cilia. Thus, the *dyf-5CA* mRNA confers substantial defects in DYF-5 protein synthesis and, at

least, its C-terminal ciliary localization domain, which prevents the kinase from phosphorylating its ciliary substrates.

Nonsense-mediated *dyf-5CA* mRNA decay

We examined the fate of *dyf-5CA* mRNAs. The A-to-I RNA editing did not create a stop codon; however, the intron-retaining transcripts often contained a premature termination codon (PTC) (fig. S7E) and might be targeted for degradation by the nonsense-mediated mRNA decay (NMD) pathway (24). Therefore, we crossed *dyf-5CA* animals with NMD mutants, including *smg-1*, a critical kinase that mediates the phosphorylation of an RNA helicase UPF1, and *smg-3*, an ortholog of human UPF2 (25, 26). The *dyf-5CA* transcripts in the *dyf-5CA*; *smg-1* double mutants became ~1.8-fold more abundant than in *dyf-5CA*, which was confirmed by using quantitative polymerase chain reaction (PCR) experiments (Fig. 3A and fig. S9A). *smg-1* or *smg-3* mutation, which did not affect WT cilia ($n > 100$), partially rescued the ciliary dye-filling defects of *dyf-5CA* (fig. S9B) and reduced IFT-particle aggregation (fig. S9, C to E), although *smg-1* mutation did not shorten the elongated cilia (fig. S9F). Blocking of NMD rescued the phenotype in Ullrich's disease by up-regulating the mRNA level of the mutant collagen subunit and forming a partially functional extracellular matrix (27). Likewise, the inhibition of NMD increases the *dyf-5CA* mRNA level, a small portion of which may translate into functional kinase, partially restoring *dyf-5CA* cilia.

RNA editing restricted two other ciliary kinases

To explore whether RNA editing restricts other kinases, we screened five kinases by overexpressing the kinase gDNA in WT. Two ciliary kinases, NEKL-4/NEK10 (never in mitosis kinase like) and DYF-18/CCRK (ortholog of human cyclin-dependent kinase 20) (28–30), when overexpressed, resulted in ciliary defects, aberrant antisense transcripts, and RNA editing on kinase pre-mRNA (Fig. 4, D to G, and fig. S10, A to D). *adr-2* deletion rescued the ciliary phenotypes in kinase overexpression (OE) animals (Fig. 4, D and E, and fig. S10, A and B), indicating that ciliary defects require RNA editing. However, we did not detect abnormalities in animal phenotypes, antisense transcripts, or RNA editing of the rest of the three cytoplasmic kinase OE strains, including the POLO kinase PLK-1, the AKT kinase family kinase AKT-1, and the adenosine monophosphate-activated protein kinase AAK-2 (fig. S11), suggesting that RNA editing may specifically regulate ciliary kinases.

Kinase hyperactivation caused aberrant RNA editing

We determined whether kinase hyperactivity or transgene overexpression caused ectopic RNA editing. Expression of a catalytic dead D609A

mutation of NEKL-4 (31) did not disrupt cilia (Fig. 4, D and E) and did not generate aberrant antisense transcription or RNA editing (Fig. 4, F and G). Similarly, the catalytically dead DYF-18(D145A) OE did not show ciliary phenotypes (fig. S10, A and B). We detected antisense transcription and RNA editing at levels similar to those of DYF-18 OE animals (fig. S10, C and D). We speculate that DYF-18(D145A) overexpression might have a residual activity in vivo, triggering RNA editing, but could not impair cilia. Consistently, the same amount of gDNA transformation disrupted cilia in 82% of NEKL-4OE but in only 23% of DYF-18OE animals (Fig. 4, D and E, and fig. S10, A and B), which suggests that the ciliary structure might be more sensitive to up-regulated NEKL-4. Furthermore, the catalytically dead DYF-5(D150A) or DYF-5(K40A) (K40A, Lys⁴⁰→Ala) (32) OE reduced the ciliary phenotype penetrance (fig. S12A), accompanying a reduction of aberrant antisense transcripts and RNA editing (fig. S12, B and C). Thus, kinase activity is a substantial cause for ciliary defects and abnormal RNA editing.

To overcome the limitation of using kinase overexpression as a proxy kinase hyperactivity, we introduced D150A in *dyf-5CA* animals (fig. S2A). DYF-5CA(D150A) protein was translated and correctly localized to cilia (fig. S12D), and *dyf-5CA(D150A)* animals did not generate any antisense transcript or RNA editing on *dyf-5* (Figs. 2B and 3, A and B), which indicated that aberrant antisense expression and RNA editing resulted from DYF-5CA hyperactivity rather than overexpression. Because of catalytic null, *dyf-5CA(D150A)* animals developed ectopically long cilia like *dyf-5* null (fig. S12D). These results support a direct contribution of kinase hyperactivity to aberrant antisense transcription and RNA editing. We suggest that transgene overexpression increased WT kinase levels, which up-regulates kinase activity, which in turn triggers antisense transcription and RNA editing of the native kinase locus.

Considering that ADR-2 is known to suppress transgene silencing through editing dsRNA that is produced from aberrant overlapping antisense transcription (33), ciliary phenotypes from kinase gDNA overexpression may involve transgene silencing. We introduced the *rde-1* (*ne219*) and *rde-4* (*ne301*) mutant alleles defective in transgene silencing (34) into *dyf-5*, *nekl-4*, and *dyf-18* gDNA OE animals, but their ciliary phenotypes were not changed (fig. S12E), suggesting that transgene silencing may not be involved.

Transcription regulation of *dyf-5CA* mRNA

dyf-5CA animals have more RNA-seq reads in the first seven exons but fewer reads in the final four exons than that of WT (Fig. 3A). We compared the stability of the *dyf-5* transcripts in WT and *dyf-5CA* animals after treatment

with actinomycin D, which blocks transcription. *dyf-5* pre-mRNAs were degraded at a similar rate in both strains (fig. S13A), which suggests that DYF-5CA may not affect transcript stability. *dyf-5CA* animals abnormally transcribe antisense RNA from the fourth exon to the seventh intron of *dyf-5*; the resultant dsRNA may inhibit RNA polymerase II (Pol II) elongation (35). To assess the potential transcriptional changes, we performed RNA Pol II chromatin immunoprecipitation followed by sequencing chromatin immunoprecipitation–sequencing (ChIP-seq). Compared with WT, *dyf-5CA* animals increased Pol II occupancy in the third to eighth exon of *dyf-5* (fig. S13B). Similar increases were observed for the elongation-specific Pol II phosphorylated at serine 2 (fig. S13B). ChIP-seq of histone H3 trimethylation at Lys³⁶ (H3K36me3) revealed increased H3K36me3 modifications in this region due to Pol II elongation and cotranscriptional deposition of H3K36me3 (fig. S13B). The increased densities indicate aberrantly high transcript elongation in the region and suggest that the lack of transcripts in the final few exons may result from transcription regulation. The *adr-2* deletion did not affect these densities in *dyf-5CA* (fig. S13B), which suggests that the increased occupancy may occur upstream or independent of RNA editing. By contrast, introducing D150A to *dyf-5CA* eliminates all the increased occupancy (fig. S13B), indicating that kinase hyperactivity causes abnormal transcription regulation.

Ciliary phenotypes in *dyf-5CA* and *dyf-5* gOE animals

Why do *dyf-5CA* animals aberrantly elongate cilia but *dyf-5* gOE worms shorten cilia? The absence of GFP fluorescence from *gfp::dyf-5CA* animals indicates that DYF-5CA protein is not produced, phenocopying the long cilia phenotype in *dyf-5* null. The *wrmScarlet::dyf-5* gOE animals produced the wrmScarlet::DYF-5 fluorescence that was incorrectly distributed around the ciliary base (fig. S14, A, B, and G). Introducing *adr-2* null into *wrmScarlet::dyf-5* gOE animals restored DYF-5 localization to the distal ciliary segments (fig. S14B) where DYF-5 is normally found, indicating that DYF-5 mislocalization owing to *dyf-5* gOE is suppressed by the loss of ADR-2. Consistently, deletion of *adr-2* rescued the short cilia defects in *dyf-5* gOE (fig. S14, C and G). Using quantitative fluorescence and quantitative real-time PCR experiments, we showed that the loss of ADR-2 does not affect the transgene expression level of *wrmScarlet::dyf-5* gOE or *osm-6::gfpOE* (fig. S14, D and E), which indicates that ADR-2 does not regulate *dyf-5* gOE phenotypes through promoting transgene expression. Because DYF-5 prevents cilia overgrowth (2), mislocalized DYF-5 at the ciliary base might have blocked

cilia elongation in *dyf-5* gOE. To test this possibility, we artificially targeted DYF-5 to the ciliary base by fusing *dyf-5* cDNA with a ciliary transition zone gene *mksr-2*. Indeed, *mksr-2::dyf-5cDNA* OE animals developed short cilia like that of *dyf-5* gOE (fig. S14, C, F, and G); however, overexpressed DYF-5 protein from *dyf-5* cDNA correctly localized at the ciliary distal and did not impair cilia (fig. S14, B, C, and G). We suggest that as long as DYF-5 localizes at the correct place, it will not generate deleterious effects, even though its amount or activity might be higher than in WT animals. In *adr-2* mutants that have increased *dyf-5CA* levels but lose RNA editing, the full-length DYF-5CA proteins with the C-terminal localization domain can be produced and properly localize at the distal ciliary segments; therefore, no shortening of cilia was observed. We speculate that *dyf-5* gOE animals expressed abundant *dyf-5* pre-mRNA, a portion of which, after RNA editing, may translate the DYF-5 kinase domain, incorrectly localizing around the ciliary base to inhibit cilia growth. By contrast, *dyf-5CA* animals expressed a much lower level of *dyf-5CA* pre-mRNA than *dyf-5* gOE, and RNA editing may severely block DYF-5CA protein production, causing aberrant cilia elongation. If the *dyf-5CA* pre-mRNA increases under certain conditions, the animal may produce truncated DYF-5 protein that localizes at the ciliary base to inhibit cilia elongation.

Cilia-to-nuclei signaling

dyf-5CA animals exhibited higher levels of *dyf-5* mRNA than WT (Fig. 3A), which suggests negative transcriptional feedback so that the loss of DYF-5 up-regulates *dyf-5* expression. We found an up-regulation of other ciliary gene expressions in the *dyf-5CA* and *dyf-5* (*mn400*) null allele and ciliary mutants that were defective in IFT-dynein CHE-3 and IFT-particle subunit DAF-10 (fig. S15 and data files S3 and S4). Flagella removal in *Chlamydomonas* caused a rapid transcription up-regulation of hundreds of flagellar-associated genes (36). Thus, a cell appears to sense whether cilia function or exist, and the “stressed” cilia may signal to the nucleus, requesting more ciliary proteins, which resembles the unfolded protein response (UPR) between the endoplasmic reticulum and the nucleus (37). Analogous to UPR regulation, an overphosphorylated ciliary protein of yet unknown identity may travel from *dyf-5CA* cilia into the nucleus to activate antisense transcription. This study describes a negative feedback loop in *dyf-5CA* animals. Given that cilia-to-nucleus signaling occurs in other ciliary mutants and deflagellated conditions, we speculate that the feedback loop elements may play roles in conditions beyond *dyf-5CA*. For example, WT worms that carry a mutation disabling the feedback loop (such as

the intron substitution *dyf-5* allele in fig. S2A) might display phenotypes under certain stressful conditions.

Discussion

We propose a model through which RNA editing restricts the hyperactive DYF-5CA ciliary kinase (Fig. 4H): (i) In response to kinase hyperactivity, antisense RNAs are transcribed in nuclei and pair with the kinase pre-mRNA. (ii) The dsRNA recruits RNA deaminase to edit kinase pre-mRNA, which changes the kinase protein sequence and impairs kinase pre-mRNA splicing. (iii) The resultant IRs generate premature stop codons, which inhibit kinase translation and activate nonsense-mediated kinase mRNA decay. (iv) The loss of kinase production converts a biochemically hyperactive kinase to loss of function in vivo, phenocopying the kinase-null cilia. Considering that *dyf-5* gOE generated more RNA editing sites on *dyf-5* locus than *dyf-5CA* (Fig. 2B), we suggest that kinase gRNA OE might involve additional regulation. However, the loss of RNA editing rescued ciliary defects under kinase gDNA OE conditions (Figs. 3C and 4, D and E, and fig. S10, A and B), underscoring the crucial role of RNA editing in safeguarding against the overactivation of kinases.

In addition to ciliary kinases, an increasing number of kinase mRNAs are hyperedited during disease progression. Examples include the protein kinase R during type I interferon responses and the CDK12 kinase mRNA from ovarian cancer cells (38–40). Although the mechanisms and impacts may differ from each of these RNAs, a parallel does emerge: RNA editing is linked to kinase hyperactivity. Recognizing this common linkage, we suggest that in response to physiological or pathological stimuli, RNA editing may target the kinase pre-mRNA, restricting kinase production and down-regulating its activity in vivo.

Our demonstration, in which suppression of RNA editing rescues ciliary defects caused by hyperactive kinases, connects cilia with other processes. Most of the ciliopathy genes are not ideal for drug development (6). We anticipate that the development of small molecules that target the pathways outside of cilia holds promise to devise strategies for the treatment of ciliopathies.

REFERENCES AND NOTES

- P. Lahiry, A. Torkamani, N. J. Schork, R. A. Hegele, *Nat. Rev. Genet.* **11**, 60–74 (2010).
- J. Burghoorn et al., *Proc. Natl. Acad. Sci. U.S.A.* **104**, 7157–7162 (2007).
- N. Vasani, J. Baselga, D. M. Hyman, *Nature* **575**, 299–309 (2019).
- S. A. Berman, N. F. Wilson, N. A. Haas, P. A. Lefebvre, *Curr. Biol.* **13**, 1145–1149 (2003).
- Y. Omori et al., *Proc. Natl. Acad. Sci. U.S.A.* **107**, 22671–22676 (2010).
- J. F. Reiter, M. R. Leroux, *Nat. Rev. Mol. Cell Biol.* **18**, 533–547 (2017).
- R. K. Ozgöl et al., *Am. J. Hum. Genet.* **89**, 253–264 (2011).

8. B. A. Tucker *et al.*, *Proc. Natl. Acad. Sci. U.S.A.* **108**, E569–E576 (2011).
9. P. D. Mace *et al.*, *Nat. Commun.* **4**, 1681 (2013).
10. Z. Fu *et al.*, *Mol. Cell. Biol.* **25**, 6047–6064 (2005).
11. L. A. Perkins, E. M. Hedgecock, J. N. Thomson, J. G. Culotti, *Dev. Biol.* **117**, 456–487 (1986).
12. G. Ou, O. E. Blacque, J. J. Snow, M. R. Leroux, J. M. Scholey, *Nature* **436**, 583–587 (2005).
13. K. Nishikura, *Nat. Rev. Mol. Cell Biol.* **17**, 83–96 (2016).
14. L. A. Tonkin *et al.*, *EMBO J.* **21**, 6025–6035 (2002).
15. M. C. Washburn *et al.*, *Cell Rep.* **6**, 599–607 (2014).
16. J. A. Arribere, H. Kuroyanagi, H. A. Hundley, *Genetics* **215**, 531–568 (2020).
17. H. Q. Zhao *et al.*, *Genome Res.* **25**, 66–75 (2015).
18. H. Ohta, M. Fujiwara, Y. Ohshima, T. Ishihara, *Genetics* **180**, 785–796 (2008).
19. D. P. Reich, K. M. Tyc, B. L. Bass, *Genes Dev.* **32**, 271–282 (2018).
20. M. B. Warf, B. A. Shepherd, W. E. Johnson, B. L. Bass, *Genome Res.* **22**, 1488–1498 (2012).
21. F. Zhang, Y. Lu, S. Yan, Q. Xing, W. Tian, *Bioinformatics* **33**, 3538–3548 (2017).
22. R. Middleton *et al.*, *Genome Biol.* **18**, 51 (2017).
23. J. Rodriguez, J. S. Menet, M. Rosbash, *Mol. Cell* **47**, 27–37 (2012).
24. T. Kurosaki, M. W. Popp, L. E. Maquat, *Nat. Rev. Mol. Cell Biol.* **20**, 406–420 (2019).
25. A. Grimson, S. O'Connor, C. L. Newman, P. Anderson, *Mol. Cell. Biol.* **24**, 7483–7490 (2004).
26. L. Johns, A. Grimson, S. L. Kuchma, C. L. Newman, P. Anderson, *Mol. Cell. Biol.* **27**, 5630–5638 (2007).
27. F. Usuki *et al.*, *Proc. Natl. Acad. Sci. U.S.A.* **110**, 15037–15042 (2013).
28. R. R. Chivukula *et al.*, *Nat. Med.* **26**, 244–251 (2020).
29. A. K. Maurya, T. Rogers, P. Sengupta, *Curr. Biol.* **29**, 1286–1300.e4 (2019).
30. K. M. Power *et al.*, *PLOS Genet.* **16**, e1009052 (2020).
31. S. H. Schmidt *et al.*, *Proc. Natl. Acad. Sci. U.S.A.* **116**, 14979–14988 (2019).
32. L. Xia *et al.*, *J. Biol. Chem.* **277**, 35422–35433 (2002).
33. S. W. Knight, B. L. Bass, *Mol. Cell* **10**, 809–817 (2002).
34. H. Tabara, E. Yigit, H. Siomi, C. C. Mello, *Cell* **109**, 861–871 (2002).
35. V. Pelechano, L. M. Steinmetz, *Nat. Rev. Genet.* **14**, 880–893 (2013).
36. A. J. Albee *et al.*, *G3* **3**, 979–991 (2013).
37. P. Walter, D. Ron, *Science* **334**, 1081–1086 (2011).
38. C. Calabrese *et al.*, *Nature* **578**, 129–136 (2020).
39. H. Chung *et al.*, *Cell* **172**, 811–824.e14 (2018).
40. J. J. Ishizuka *et al.*, *Nature* **565**, 43–48 (2019).

ACKNOWLEDGMENTS

We thank J. Reiter, X. Yang, V. Ambros, D. Xue, Z. Lu, X. Shen, Y. Qi, S. Cai, and Y. Wang for discussion. **Funding:** This work was supported by the following funding programs: National Natural

Science Foundation of China (grants 31991190, 31730052, 31525015, 31861143042, 31561130153, 31671444, and 31871352) and National Key R&D Program of China (2017YFA0503501, 2019YFA0508401, and 2017YFA0102900). **Author contributions:** D.L., P.Y., Z.Z., W.L., Q.C.Z., J.B.L., and G.O. conceived and designed the project. D.L., Z.Z., and P.Y. performed research; D.L. and Y.L. analyzed data; D.L., Z.Z., W.L., Q.C.Z., J.B.L., and G.O. wrote the paper. **Competing interests:** G.O., W.L., D.L., Z.Z., and P.Y. are inventors on patent application no. CN202110893049.4, submitted by Tsinghua University, that covers applications of RNA editing on genetic disorders that are associated with gain-of-function proteins. **Data and materials availability:** All data are available in the main text or supplementary materials. All sequencing data from this study have been submitted to the NCBI Sequence Read Archive (SRA; www.ncbi.nlm.nih.gov/sra) with BioProject accession number PRJNA655606.

SUPPLEMENTARY MATERIALS

science.sciencemag.org/content/373/6558/984/suppl/DC1

Materials and Methods

Figs. S1 to S15

Tables S1 to S5

References (41–47)

MDAR Reproducibility Checklist

Data S1 to S4

24 August 2020; resubmitted 1 April 2021

Accepted 16 July 2021

10.1126/science.abd8971



Supplementary Materials for
RNA editing restricts hyperactive ciliary kinases

Dongdong Li *et al.*

Corresponding author: Guangshuo Ou, guangshuou@tsinghua.edu.cn

Science **373**, 984 (2021)
DOI: 10.1126/science.abd8971

The PDF file includes:

Materials and Methods
Figs. S1 to S15
Tables S1 to S5
References

Other Supplementary Material for this manuscript includes the following:

MDAR Reproducibility Checklist
Data S1 to S4

Materials and Methods

Worm strains and culture

C. elegans were maintained according to the standard methods (Brenner, 1974). All worms were cultivated at 20 °C on nematode growth medium (NGM) plates seeded with the *Escherichia coli* OP50 unless stated otherwise. Young adult hermaphrodite worms were used in the dye-filling assays and live-cell imaging experiments. The wild-type strain was Bristol N2. Some strains were provided by the *Caenorhabditis* Genetics Center (CGC), which is funded by the NIH Office of Research Infrastructure Programs (P40 OD010440). Table S1 summarizes the strains used in this study.

Molecular biology

We followed the established protocols to perform the genome editing experiments in *C. elegans* (Dickinson et al., 2013; Friedland et al., 2013). We used the CRISPR design tool (<https://zlab.bio/guide-design-resources>) to select the target sequence. The sgRNA sequences (Table S2) were inserted into the pDD162 vector (Addgene, #47549) by linearizing this vector with 15 bp overlapped primers. The resulting PCR products containing 15 bp overlapped double-strand DNA ends were treated with DpnI digestion for 4 hours and transformed into *E. coli*. The linearized PCR products were cyclized to generate plasmids by spontaneous recombination in bacteria. For fluorescence tag knock-in, homology recombination (HR) templates were constructed by cloning the homology arms into pPD95.77 plasmids using In-Fusion Advantage PCR cloning kit (Clontech, #639621). Subsequently, fluorescence tag sequences were inserted into the constructs with a flexible linker before the stop codons or after the start codon ATG. Target sites in the templates were modified with synonymous mutations. To knock-in point mutations, we constructed the mutation sites with synonymous mutations to acquire the specific restriction enzyme recognition sites on the HR templates by In-Fusion Advantage PCR cloning kit. All the plasmids and primers were listed in Table S3.

Genome editing

CRISPR-Cas9 constructs and HR templates were purified with AxyPrep Plasmid Purification Miniprep Kit (Axygen, #AP-MN-P-250) and PureLink Quick PCR purification Kit (Invitrogen, #K310001) and co-injected into the gonads of young adult worms with the *rol-6(su1006)* and *Podr-1::dsRed* selection markers. F1 transgenic progenies were singled and screened by PCR using EasyTaq® 2× Super Mix (TransGen Biotech, #AS111-14). In our screen for knock-in animals that carry the point mutation, we performed an additional restriction enzyme digestion step before gel electrophoresis. All variations were verified by the Sanger sequencing of the entire genes, and no other mutations were inserted on the target genes.

Microinjection and transgenic strains

For transgenic *C. elegans* experiments, transgenic lines were generated by injecting the DNA constructs into the gonads of the indicated worm strains. The co-injected selection marker was *rol-6*. At least two independent transgenic lines with a constant transmission rate (>50%) were propagated. Concentrations of DNA constructs used for generating knock-in were 50 ng/μl, and for overexpression was 20 ng/μl.

Dye-filling assay

The fluorescence dye DiI filling assay was widely used to assess the ciliary function and integrity (Hedgecock et al., 1985; Perkins et al., 1986; Starich et al., 1995). Animals that are dye-filling defective develop abnormal ciliary structures and are defective in the animal behavioral assays, such as the osmotic avoidance assay and chemotaxis assay (Hedgecock et al., 1985; Inglis et al., 2007; Perkins et al., 1986; Starich et al., 1995). Young adult worms were harvested into 100~200 μ L M9 buffer and mixed with equal volume dyes (DiI 1,1'-dioctadecyl-3,3,3',3'-tetramethylindo-carbocyanine perchlorate, Sigma) at the working concentration (20 μ g/ml), followed by incubation at room temperature in the dark for 30 min. Worms were then transferred to seeded NGM plates and examined for dye uptake two hours later using a fluorescence stereoscope or fluorescence compound microscopes. We observed at least 50 animals of each strain from three independent assays.

Forward genetic screens

We used forward genetic screens to isolate *dyf-5CA* suppressors. The *dyf-5CA* (*cas501*) mutant animals (P0) were synchronized at the late L4 larval stage, collected in 4 mL M9 buffer, and incubated with 50 mM ethyl methanesulfonate (EMS) for 4 hours at room temperature with constant rotation. Animals were then washed with M9 three times and cultured under standard conditions. After 20 hours, adult animals were bleached. Eggs (F1) were distributed and raised on ~100 9-cm NGM plates, each containing 50 to 100 eggs. Adult F2 animals on each plate were collected and subjected to dye filling (see Dye-filling assay below). Dye-positive mutant animals were individually cultured, and their progenies were further examined via the dye-filling assay. Using the single nucleotide polymorphisms (SNPs), we mapped *cas506* at -1.69~1.66 cM on chromosome III. We identified mutations using whole-genome sequencing. We confirmed gene cloning using multiple alleles and rescue experiments.

Mass spectrometry

GFP transgenic or knock-in strains raised on 100 90-mm NGM plates were collected and washed three times with M9 buffer. Lysates were made from 1~2 mL packed worms in lysis buffer (25 mM Tris-HCl, pH 7.4, 150 mM NaCl, 1% NP-40, 10% glycerol, 1x cocktail of protease inhibitors from Roche (Complete, EDTA free), 40 mM NaF, 5 mM Na₃VO₄) and 3~4 mL of 0.5-mm diameter glass beads using FastPrep-24 (MP Biomedicals). Proteins were immunoprecipitated with GFP-Trap A beads (Chromotek) and eluted with 300 μ l 0.1 M glycine-HCl (pH 2.5) into 15 μ l 1.5 M Tris-HCl (pH 8.8), followed by precipitation with 100 μ l trichloroacetic acid and re-dissolving in 60 μ L 8 M urea, 100 mM Tris-HCl (pH 8.5). Samples were treated with 5 mM TCEP for reduction, 10 mM iodoacetamide for alkylation, and then diluted fourfold with 100 mM Tris-HCl (pH 8.5). The proteins were digested with 0.2 μ g trypsin at 37°C overnight after the addition of 1 mM CaCl₂ and 20 mM methylamine, and the resultant peptides were desalted with ZipTip pipette tips (Merck Millipore). For liquid chromatography-tandem mass spectrometry analysis, peptides were separated by a flow rate of 0.25 μ l/min using an EASY-nLCII integrated nano-HPLC system (Proxeon, Odense, Denmark), which was directly interfaced to a Thermo Scientific Q Exactive mass spectrometer. The analytical column was a fused-silica capillary column (75 μ m in internal diameter, 150 mm in length; Upchurch) packed with C-18 resin (300 Å, 5 μ m; Varian). Mobile phase A consisted of 0.1% formic acid, and mobile phase B consisted of 100% acetonitrile and 0.1% formic acid. The Q Exactive mass spectrometer was operated in data-dependent acquisition mode using Xcalibur 2.1.2 software. There was a single full-scan mass spectrum in the

orbitrap (400–1,800 m/z , 60,000 resolution) followed by ten data-dependent tandem mass spectrometry scans at 27% normalized collision energy (HCD). The tandem mass spectrometry spectra were searched against the *C. elegans* proteome database using the Proteome Discoverer (version PD1.4; Thermo Fisher Scientific).

Imaging

Young adult *C. elegans* hermaphrodites were anesthetized with 0.1 mM/L levamisole in M9 buffer, mounted on 3% agarose pads, and maintained at room temperature. Imaging was performed using a Zeiss Axio Observer Z1 microscope equipped with 405, 488, and 561 laser lines, a Yokogawa spinning disk head, an Andor iXon+ EM-CCD camera, and a Zeiss 100 \times /1.46 objective. Images were acquired by μ Manager (<https://www.micro-manager.org>). All the images were taken using identical settings. Image analysis and measurement were performed with ImageJ software (<http://rsbweb.nih.gov/ij/>). Image stacks were z-projected using maximum projection. We used an established protocol to measure cilia length and determine the speeds of intraflagellar transport with the ciliary marker IFT52/OSM-6::GFP (Ou et al., 2005). To quantify the endogenous DYF-5 fluorescence intensity, we acquired the images within the same day under identical settings, and the signal was the GFP::DYF-5 fluorescence minus the background fluorescence. To quantify the exogenous DYF-5 or OSM-6 fluorescence intensity, we acquired the images within the same day under identical settings, image stacks were z-projected using average projection, and the signal was the wrmScarlet::DYF-5 or OSM-6::GFP fluorescence minus the background fluorescence.

Sequence alignment

Sequence alignment was performed using Clustal X2.1 (<http://www.clustal.org/>). Protein sequences were obtained from Wormbase (<http://www.wormbase.org/>) or National Center for Biotechnology Information (www.ncbi.nlm.nih.gov/). Conserved domains were identified by SMART (simple modular architecture research tool) (<http://smart.embl-heidelberg.de/>) or CDD (NCBI's conserved domain database) online tools. Sequence IDs used include CE46107 (*CeDYF-5*), NP_005897.1 (*HsMAK*), NP_001139275.1 (*MmMAK*), NP_956240.1 (*DrMAK*), AAO86687.1 (*CrLF4*), CE25120 (*CeADR-2*), CE32459 (*CeADR-1*), NP_001351974.1 (*HsADAR1*), NP_001103.1 (*HsADAR2*), NP_001139768.1 (*MmADAR1*), NP_570965.2 (*MmADAR2*), NP_569940.2 (*DmdADAR*), NP_001362329.1 (*HsICK*), NP_055041.1 (*HsMOK*), NP_004187.3 (*HsCDKL1*), NP_001317653.1 (*HsCDKL2*), NP_001107047.1 (*HsCDKL3*) and M84489.1 (*HsERK2*). The full-length sequences were used to perform alignment.

RNA sequencing

Synchronized worms were cultured on NGM plates without the OP50 bacteria. Worms were harvested at the L1 larval stage and then lysed with TRIzol reagent (Invitrogen). Total RNA was extracted according to the manufacturer's protocol. SUPERase•InTM RNase Inhibitor (Invitrogen) was used in each step to prevent RNA from degradation. RNA concentration was quantified using the Qubit RNA High Sensitivity Assay Kit (Invitrogen). RNA quality was assessed with the Agilent 2100 bioanalyzer system, and samples with an RNA integrity number (RIN) above 6.0 were used to construct the library. 50 ng to 500 ng of total RNA was used for library preparation using the KAPA RNA HyperPrep Kit (KAPA Biosystems). Library samples were analyzed by Agilent 2100 bioanalyzer system and Qubit for quality control and quantification. The samples were sequenced on an Illumina HiSeq platform. A total of 150-bp paired-end reads were generated.

Gene expression analysis

The resulting raw reads were assessed for quality, adaptor content, and duplication rates with FastQC. The raw sequencing reads were trimmed using Trim_galore (version 0.4.4) to remove the low-quality bases and adaptor sequences. Paired-end reads with at least 20 nucleotides in length were aligned to *C. elegans* reference genome (ce10) using STAR (2.5.4b) with the parameter ‘—sjdbOverhang 139’. The numbers of reads that aligned to genes were quantified by HTSeq (version 0.9.1). Only uniquely mapped reads were used to calculate the relative expression level of the gene. Reads overlapping with multiple genes or aligning to multiple regions were excluded. Gene names were annotated on the DAVID website (<https://david.ncifcrf.gov/>). Differentially expressed genes were identified using DESeq2 package in R programming language, and differentially expressed genes were defined with the following criteria: up-regulated genes (false discovery rate (FDR) less than 0.05, log₂-transformed fold change greater than 1, un-normalized counts from HTSeq greater than 3); downregulated genes (FDR less than 0.05, log₂-transformed fold change less than -1, and un-normalized counts from HTSeq greater than 3); and other genes representing the ones that are not differentially expressed. Metascape (<http://metascape.org/gp/index.html>) was used to identify gene enrichment terms in up-regulated or down-regulated genes. We used the ggplot2 package of R to plot figures.

RNA editing analysis

We used the SPRINT (SNP-free RNA editing Identification Toolkit) method to identify RNA editing sites (Zhang et al., 2017). In brief, trimmed and filtered RNA-seq reads were mapped to the *C. elegans* reference genome (ce10) using BWA (version 0.7.12). The Samtools (version 1.2) was applied to convert SAM files to BAM files and sort BAM files. The Picard-tools (version 1.119) were used to remove PCR duplicates. Uniquely mapped read pairs were retained for further analyses. Unmapped reads and the reference genome were masked by replacing A with G and replacing T with C, and remapped reads were obtained by recovering remapped masked reads. SNVs calling was performed with repeat annotation (ce10). Further RNA editing sites (RES) were called. Our study defines the RES with support reads that are greater than 3. We used the seaborn packages of Python and the ggplot2 package of R to plot figures.

Antisense RNA analysis

Analysis of antisense RNA starts with the raw strand-specific RNA-seq data formatted as FASTQ files. Raw reads were quality and adapter trimmed using Trim_galore before alignment. Trimmed reads were aligned using STAR (2.5.4b) with the default parameters against the *C. elegans* genome ce11 from UCSC. Reads mapped to the forward, or reverse strand were extracted from BAM files acquired from STAR using Samtools with the following parameters: ‘view -f 16 -F 4 -b’ for the reverse strand and ‘view -F 16 -F 4 -b’ for the forward strand. The separated BAM files were intersected with the reverse and forward GTF files using BEDTools to acquire antisense and sense reads mapped to the forward and reverse strands, respectively. BAM files were merged according to the forward and reverse strands using Samtools. We used HTSeq to quantify read counts from BAM files.

Reverse transcription and quantitative real-time PCR

cDNA was synthesized in a 20 µl reaction volume using the RevertAid First Strand cDNA Synthesis Kit (Thermo Scientific). 2 µl of 1:4 dilution of cDNA was used as the template in a 20 µl reaction volume from the PowerUp SYBR Green Master Mix (Applied Biosystems). A list of

the real-time PCR primers is in the resource Table S4. Quantitative real-time PCR was performed in three replicates using the Applied Biosystems QuantStudio 1 Real-Time PCR System and normalized to the actin gene *act-5*. Data were analyzed using the standard curve method. The experiments were repeated three times on independent RNA preparations.

Quantification of intron retention

The IRFinder from Middleton et al. was applied to estimate intron retention in each sample (Middleton et al., 2017). The package is available from GitHub (<https://github.com/williamritchie/IRFinder/wiki>). In general, reads are mapped to the reference genome by STAR using default scoring parameters but excluding multi-mapping reads from the output. The default scoring parameters suit IR's detection as they favor neither mapping from exon to exon across splice junctions nor mapping from exons into introns. IR is determined by the measurement of both the splicing level and intronic abundance. The calculated metric is the IR ratio. Both the exonic and intronic abundance are normalized for feature-length. Normalization for library size is not required as intronic and exonic abundance are measured from the same data. The IR ratio is calculated simply as intronic abundance divided by the sum of intronic abundance and normal splicing abundance.

Measurement of RNA stability

For transcription inhibition, Actinomycin D (Act D) (Sigma Aldrich, Saint Louis, Missouri) was added to M9 supplemented with DMSO alone or 200 µg/ml Actinomycin D in DMSO. Worms at mixed stages were placed in M9 supplemented with or without Act D, and then collected for different times (0, 1, 2, 3, 4 hours) at 20 °C for analysis. Total RNA was extracted with TRIzol reagent. cDNA was synthesized in a 20 µl reaction volume using the PrimeScript RT Reagent Kit with gDNA Eraser (TaKaRa). 2 µl of 1:4 dilution of cDNA was used as the template in a 20 µl reaction volume from the PowerUp SYBR Green Master Mix (Applied Biosystems). Data were normalized to the expression of a control gene *act-5*, and DMSO treated samples for each experiment. A list of the real-time PCR primers is in the resource Table S5.

Chromatin immunoprecipitation

For ChIP assays, chromatin immunoprecipitation was performed as described (Mukhopadhyay et al., 2008) with modifications. Briefly, worms were harvested and washed several times in M9 buffer and washed twice in phosphate-buffered saline (PBS). Worms were lysed in cross-linking buffer (1% formaldehyde in PBS with a proteinase-inhibitor cocktail) for 30 min at room temperature. Fixed worm samples were quenched with 0.125 M glycine and washed in cold PBS buffer with protease inhibitors three times. Samples were resuspended in ice-cold FA buffer (50 mM HEPES-KOH pH 7.5, 150 mM NaCl, 1 mM EDTA, 0.1% sodium deoxycholate, 1% Triton X-100, 1 mM PMSF, and the protease inhibitor cocktail) with 0.1% SDS, and sonicated using a Covaris sonication system. The sonicated samples were centrifuged at 12,000 rpm for 15 min at 4 °C. Chromatin samples were incubated with specific antibodies overnight at 4 °C. The protein-DNA complexes were immobilized on pre-washed protein A/G beads. After proteinase K digestion and reverse cross-linking, the precipitated DNA and input DNA were purified using phenol/chloroform, precipitated with ethanol, and subjected to DNA library construction. The antibodies used were RNAPII (SCBT, sc-56767), RNAPII Ser2P (CST, 13499), and H3K36me3 (Abcam, ab9050).

ChIP-seq data analysis

The resulting raw reads were assessed for quality, adaptor content, and duplication rates with FastQC. The raw sequencing reads were trimmed using Trim_galore (version 0.4.4) to remove the low-quality bases and adaptor sequences. Clean reads were aligned to *C. elegans* reference genome (ce10) using BWA aligner (version 0.7.17) with default parameters. ChIP-seq peaks were called using MACS software (version 2.2.7.1) with the default parameters. BigWig files were generated using the deeptools with the RPKM normalization method.

Protein Purification

Recombinant GST-DYF-5KD (Kinase Domain), GST-DYF-5KD(T164E), and GST-IFT-74N (N-terminus) were purified from the *E. coli* BL21 (DE3) strain using the standard affinity purification protocols. Purified proteins were dialyzed against storage buffer (50 mM Tris-HCl, pH 8.0), frozen in liquid nitrogen, and stored at -80°C .

In Vitro Phosphorylation Assays

20 μM IFT-74N was incubated with 0.5 μM DYF-5KD or DYF-5KD(T164E) at 30°C in 100 μl of reaction mixture containing 50 mM Tris-HCl pH 8.0, 10 mM MgCl_2 , 150 mM NaCl, and 2 mM ATP. We saved 20 μl samples from the reaction system at the following time: 0 min, 15 min, 30 min, 60 min, and 120min. The reaction was terminated by boiling the sample for 5 min with an SDS-sample buffer. We resolved the samples by SDS-PAGE followed by immunoblotting using an anti-GST antibody (Easybio, BE2065) to monitor IFT-74N, DYF-5KD, or DYF-5KD(T164E) and by using an anti-pSTY antibody (CST, 9381) to monitor phosphorylated serine, threonine, or tyrosine.

Data reporting and statistics

No statistical methods were used to predetermine the sample size. The sample sizes in our experiments were determined from the related published analyses. The experiments were not randomized. All *C. elegans* strains were synchronized and cultivated at 20°C . We used GraphPad Prism 7 (GraphPad Software, Inc.) for statistical analyses. Independent Student's t-tests were performed to compare the mean values between the two groups. Statistic significances were designated as *, $p < 0.05$; **, $p < 0.01$; and ***, $p < 0.001$. We provided the information about statistical tests, P values, and n numbers in the respective figures and figure legends.

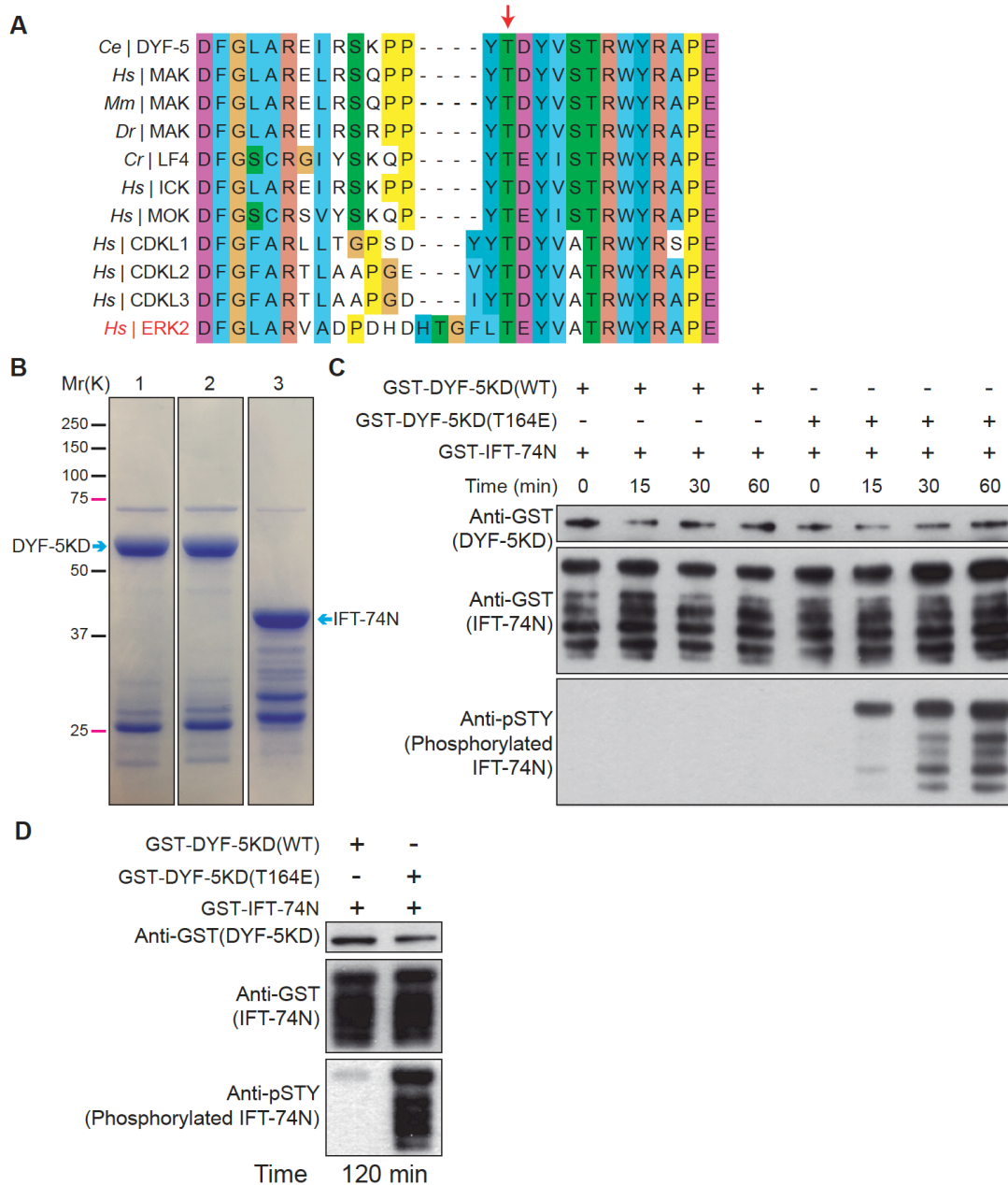


Fig. S1. The constitutive kinase activity of DYF-5(T164E).

(A) Multi-sequence alignment of the *C. elegans* (Ce) DYF-5 kinase and its homologs and other MAP kinases in human (Hs), mouse (Mm), zebrafish (Dr), and *Chlamydomonas* (Cr). ERK2 is highlighted in red. The arrow highlights the phosphorylated Threonine residues to achieve full kinase activity. (B) Coomassie-stained SDS-PAGE analysis of recombinant GST-DYF-5KD (Kinase Domain, 11-291 aa) (1), GST-DYF-5KD(T164E)(11-291 aa) (2), and GST-IFT-74N(1-133 aa) (3). Mr, relative molecular weight; K, thousands. KD, kinase domain. N, N-terminus. (C-D) Recombinant GST-IFT-74N (20 μ M) was used as a substrate in an in vitro kinase assay with GST-DYF-5KD (0.5 μ M) and GST-DYF-5KD(T164E) (0.5 μ M) purified from the *E. coli* BL21 (DE3) strain. Phosphorylation of IFT-74N by DYF-5KD and DYF-5KD(T164E) for the indicated time (C) or two hours in (D) was analyzed using an anti-pSTY antibody.

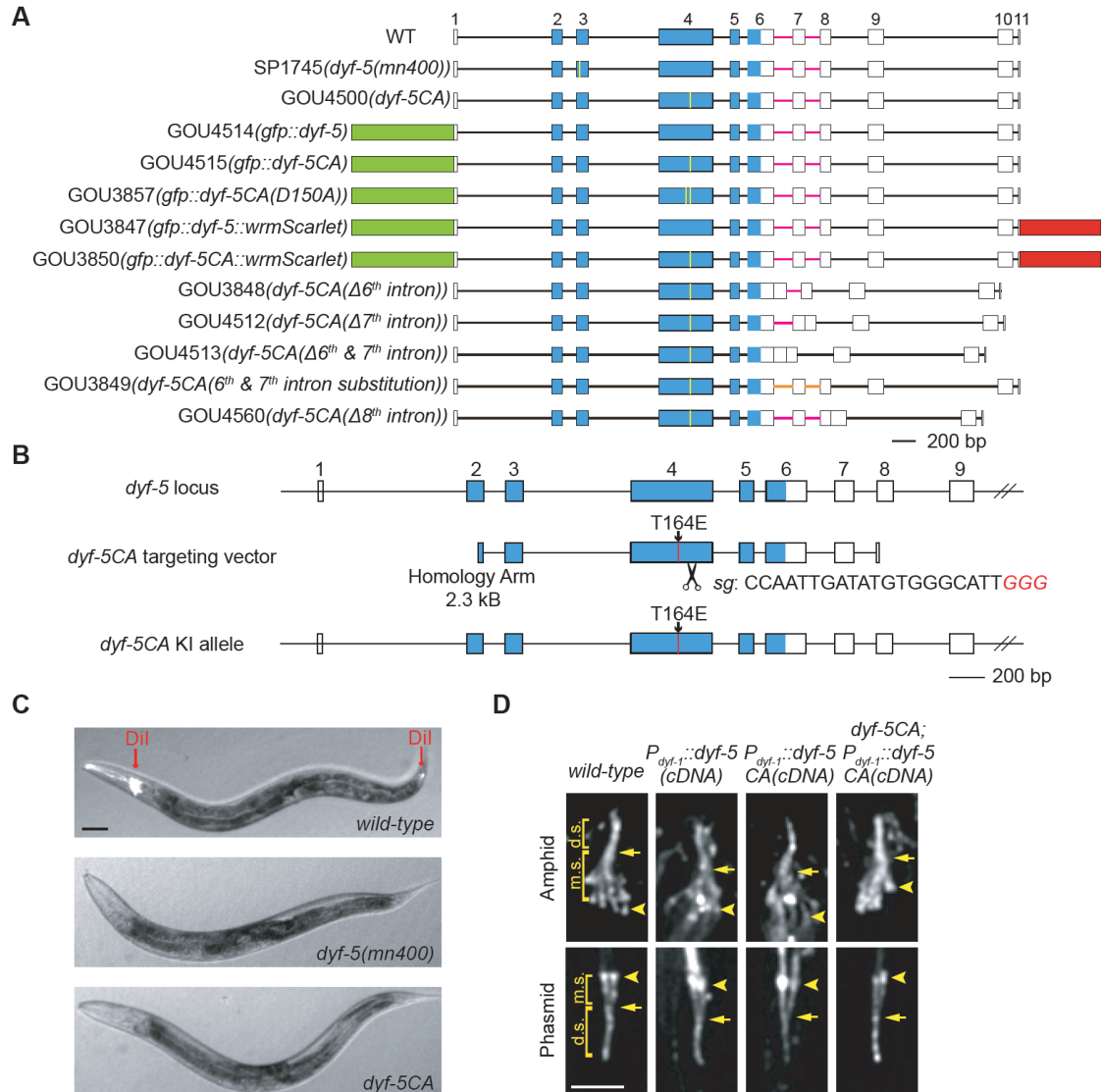


Fig. S2. Summary of *dyf-5* mutations and strains.

(A) Summary of *dyf-5* strains. The green and red rectangles show the GFP and wrmScarlet, respectively. Yellow vertical lines indicate the point mutation W49* (the reference null allele *mn400*), T164E, or D150A. The 6th and the 7th introns are in pink, and the replaced 6th and the 7th introns are in orange. (B) Schematic of the *dyf-5CA* knock-in allele using the CRISPR-Cas9-based genome editing strategy. Rectangles filled with blue color show the DYF-5 kinase domain. Scissors show the Cas9 cleavage site, with the single-guide RNA (sgRNA) target sequence on the right and the PAM (protospacer adjacent motif) sequence in red. Red lines within the 4th exon located blue rectangle show the T164E mutation site. A 2.3 kb homology arm was inserted into the plasmid pPD95.77 to generate a homology recombination (HR) template. (C) Dye-filling of *wild-type* (upper), *dyf-5(mn400)* (middle) and *dyf-5CA* (lower) animals. Both the null allele *dyf-5(mn400)* and *dyf-5CA* animals are dye-filling defective. Anterior is to the left. (D) Ciliary phenotypes in the indicated strains were visualized using GFP-tagged IFT52/OSM-6. Arrowheads indicate the ciliary base and transition zone, and arrows indicate junctions between the middle and distal segments. The scale bar is 5 μm.

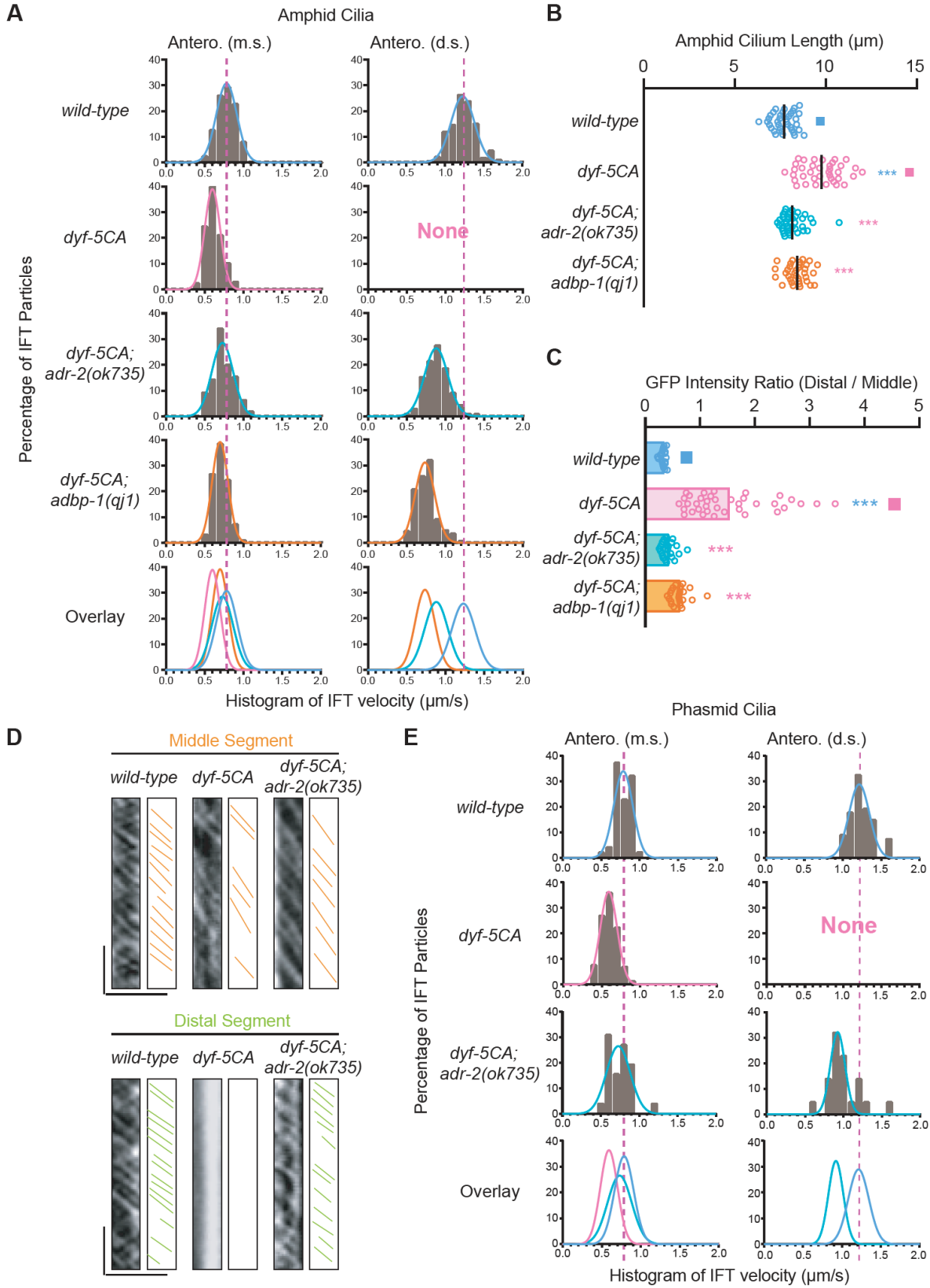


Fig. S3. DYF-5CA disrupted intraflagellar transport (IFT).

(A) Histogram of IFT velocities in amphid sensory cilia. Left: anterograde IFT in the middle segments; right: anterograde IFT in the distal segments. A Gaussian distribution fits each plot. m.s., middle segment; d.s., distal segment. (B) Cilium length of amphid sensory cilia in the indicated strains, N = 30 – 60. Statistical significance compared with the control with a matching color code is based on Student's t-test, n.s., not significant, * $p < 0.05$, ** $p < 0.01$, *** $p < 0.001$. (C) Fluorescence ratio of GFP-tagged IFT52/OSM-6 between the distal and the middle amphid ciliary segments in different genotypes. The high fluorescence in the distal ciliary portions of *dyf-5CA* animals indicates the aggregation of IFT-particles marked by IFT52/OSM-6::GFP, whereas mutations of *adr-2* or *adbp-1* reduced the aggregations. N > 20 for each genotype. (D) Kymographs show IFT-particle movement along the middle ciliary segment (upper) or distal segment (lower) of phasmid cilia in *wild-type* and mutants. Representative particle traces are marked with orange and green lines. Scale bars represent 5 μm (horizontal) and 5 sec (vertical). (E) Histogram of IFT velocities in phasmid sensory cilia. Left: anterograde IFT in the middle segments; right: anterograde IFT in the distal segments. A Gaussian distribution fits each plot.

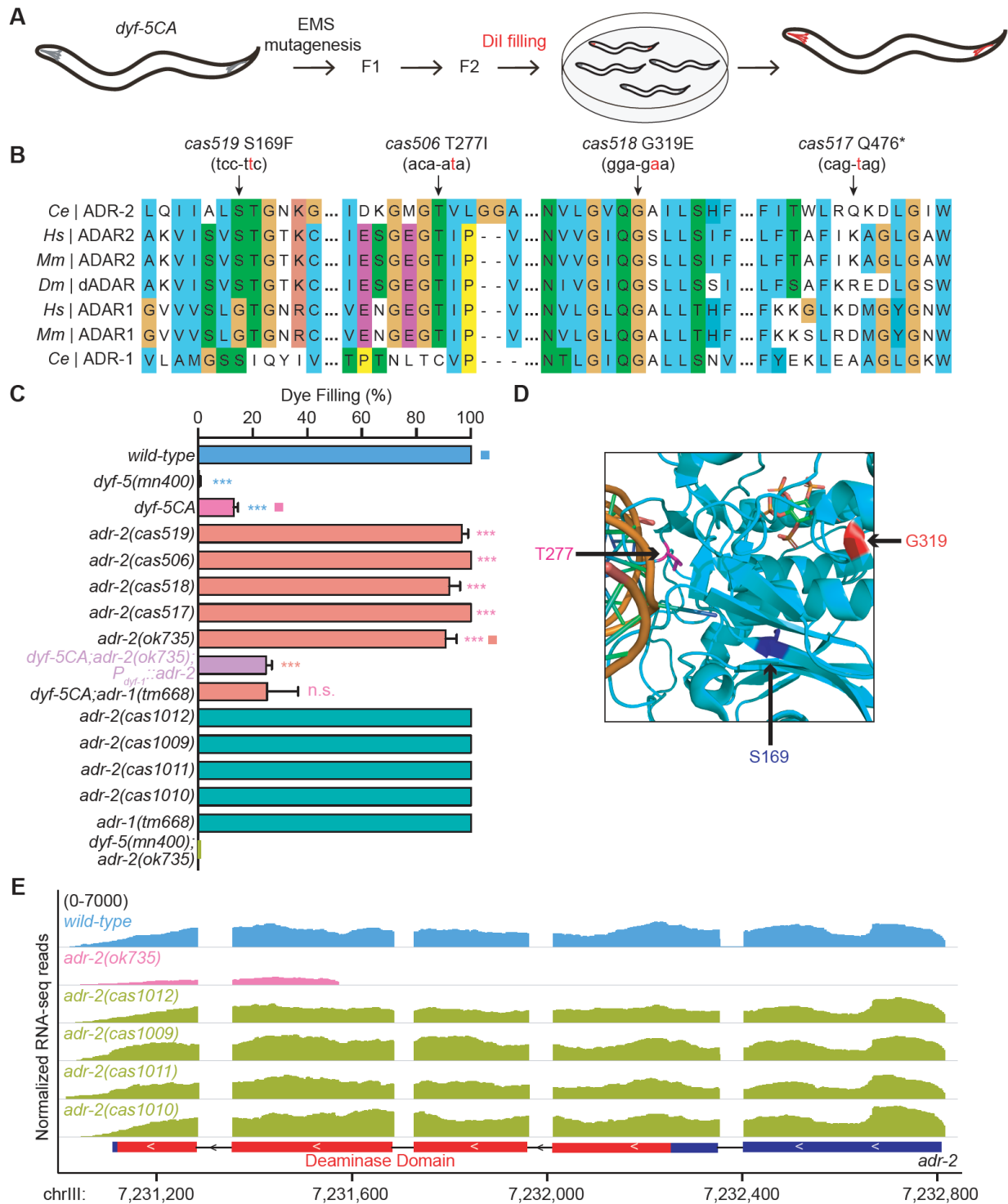


Fig. S4. Genetic suppressor screens identified that ADR-2 mutations rescued ciliary defects in *dyf-5CA* animals.

(A) Flowchart of the suppressor screening. *dyf-5CA* animals are dye-filling defective (Dyf). Animals at the late L4 stage were mutagenized with ethyl methanesulfonate (EMS). F2 progenies were screened using the dye-filling assay. Dye-positive animals were candidate suppressors. The

mutant gene was cloned by single-nucleotide polymorphism mapping combined with whole-genome sequencing. **(B)** Multi-sequence alignment of *C. elegans* (Ce) ADR-2 with ADR-1 and its homologs in human (Hs), mouse (Mm), *Drosophila* (Dm), and *Chlamydomonas* (Cr). Arrows highlight mutations isolated from our screens, and the mutated nucleotides are shown in red. **(C)** Percentage of dye-filling positive in the indicated strains. N = 100 – 200. Mean \pm SD (error bars). Statistical significance compared with the control with a matching color code is based on Student's t-test, n.s., not significant, * $p < 0.05$, ** $p < 0.01$, *** $p < 0.001$. **(D)** Conserved ADR-2 mutation sites (S169F, T277I, and G319E) from the EMS screen are shown in the human ADAR2 protein X-ray structure (PDB: 5ED1). **(E)** Distributions of normalized RNA-seq reads at the *adr-2* locus in *wild-type* animals and *adr-2* mutants are displayed in IGV. The *adr-2(ok735)* deletion allele is a putative null mutant, and the point mutation alleles do not affect the *adr-2* mRNA expression level. Gene bodies and genomic locations are represented below the track sets; red boxes, deaminase domain. RNA-seq signals are shown in the range (0-7000).

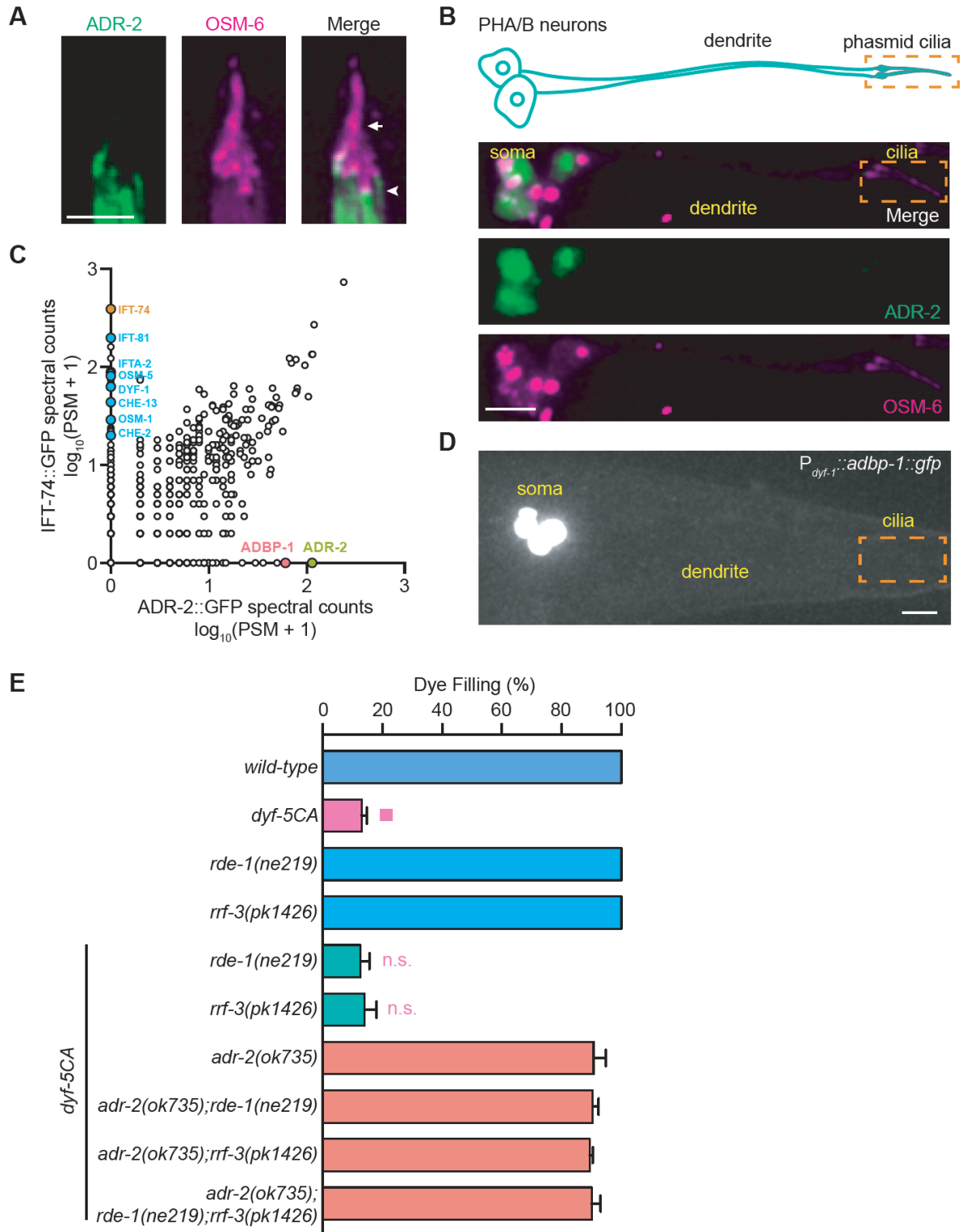


Fig. S5. ADR-2 and ADBP-1 proteins in sensory neurons.

(A) Localization of ADR-2 in amphid (A) and phasmid (B) sensory neurons. ADR-2::GFP was expressed under the control of the ciliated neuron-specific *P_{dyf-1}* promoter. Cilia were marked with mCherry-tagged IFT52/OSM-6. No green fluorescence was detected in cilia. (B) Schematic

diagram of phasmid ciliated sensory neurons in *C. elegans*. Anterior is to the left, and the dashed box indicates the phasmid cilia (upper). Localization of ADR-2 in nuclei but not in cilia (lower). (C) Mass spectrometric analysis of proteins purified by anti-GFP agarose beads from transgenic worms expressing ADR-2::GFP or an IFT-particle protein IFT-74::GFP knock-in worms. The plot compares proteins co-precipitated with ADR-2::GFP or the control IFT-74::GFP. IFT-74::GFP affinity purification pulled down other IFT proteins, including IFT-particle subunits (blue along the Y-axis), whereas ADR-2::GFP pulled down ADBP-1 but not ciliary proteins (X-axis). (D) Localization of ADBP-1 in nuclei but not in cilia of the phasmid neurons. ADBP-1::GFP was expressed under the control of the *Pdyf-1* promoter. (E) Percentage of dye-filling in *wild-type* and mutants. N = 200 – 300. Mean \pm SD (error bars). Statistical significance compared with the control with a matching color code is based on Student's t-test, n.s., not significant, * $p < 0.05$, ** $p < 0.01$, *** $p < 0.001$. Scale bars, 5 μ m.

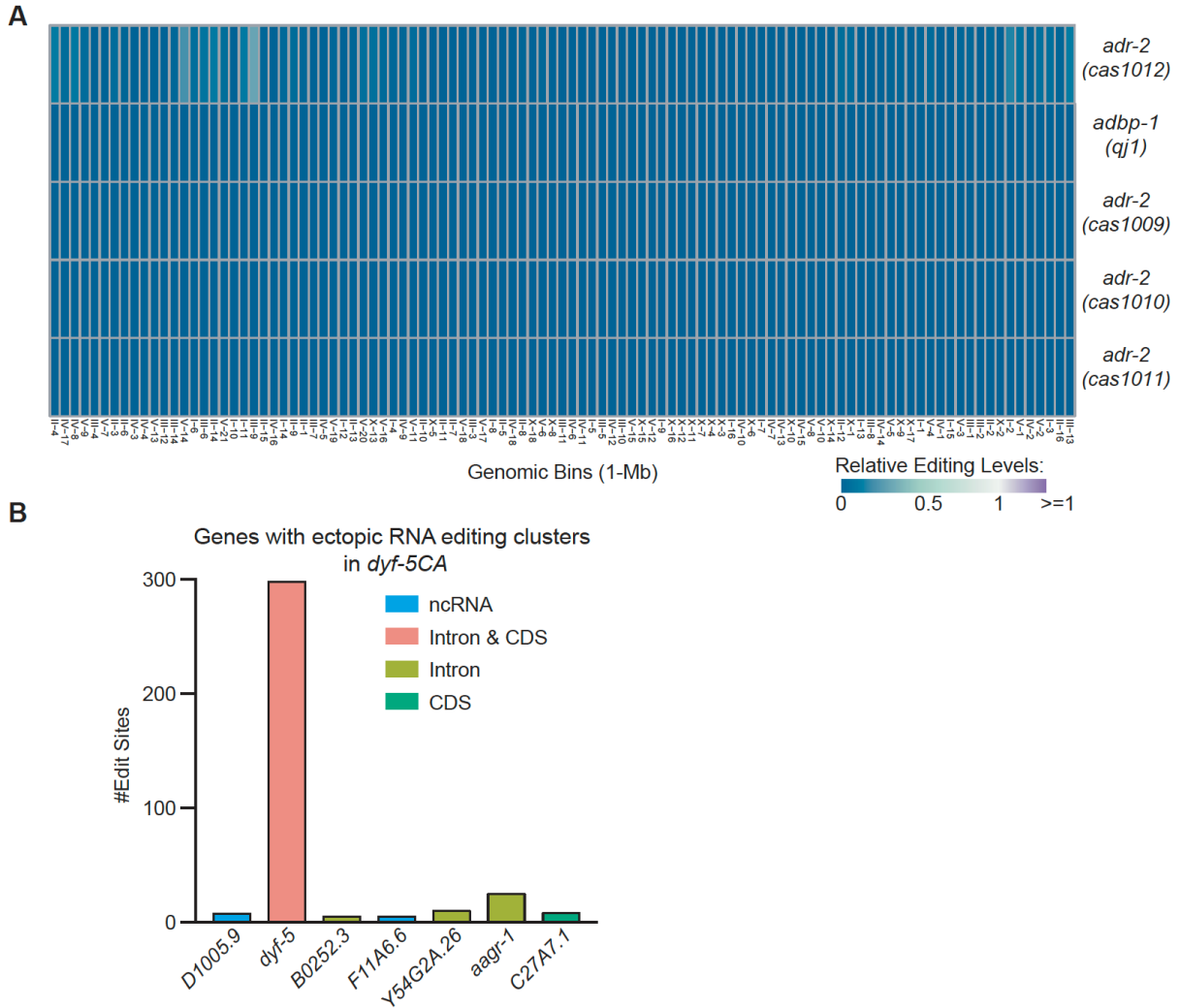


Fig. S6. RNA editing in *dyf-5CA* animals.

(A) Heat map and dendrogram of hierarchical clustering of editing sites using editing ratios among *adr-2* and *adbp-1* L1 larvae in different genomic bins (1-Mb tile). Relative editing levels were used in hierarchical clustering. Each row corresponds to a sample. Each column represents the relative editing ratio in a genomic bin. Experiments were repeated three times with similar results. (B) The number of editing sites among genes that do not have any RNA editing sites in *wild-type* but gain ectopic RNA editing clusters in *dyf-5CA* animals. Different colors distinguish the location of RNA editing sites.

Fig. S7. RNA editing of the *dyf-5CA* pre-mRNA causes ciliary defects.

(A) Schematic of deletion or replacement of the 6th and the 7th introns in *dyf-5CA* knock-in allele using the CRISPR-Cas9-based genome editing strategy. The rectangles filled with blue color show the DYF-5 kinase domain. Scissor shows the Cas9 cleavage site, with the single-guide RNA (sgRNA) target sequence above and the PAM (protospacer adjacent motif) sequence in red. Redlines within the 4th exon located blue rectangle show the T164E mutation site. A 7.0 kb homology arm was inserted into the plasmid pPD95.77 to make the homology recombination (HR) template. (B) Ciliary phenotypes in *dyf-5CA* animals visualized using IFT52/OSM-6::GFP. The scale bar is 5 μ m. (C) The nucleotide sequences of the 6th and 7th introns in *wild-type* and intron substitution animals. Thymine highlighted in red indicates the replaced Adenosine that was edited in *dyf-5CA* animals. The splicing donor and acceptor sites were underlined in blue. (D) The amino acid sequence of DYF-5 in *wild-type* or *dyf-5CA* mutant animals. RNA editing sites in the 6th and the 7th exons of *dyf-5* changed the DYF-5 protein sequence in *dyf-5CA* animals. Red asters show the mutation sites. (E) The amino acid sequence of DYF-5 in *wild-type* or mutants with the 6th or the 7th intron retentions. Red asters show the premature stop codons.

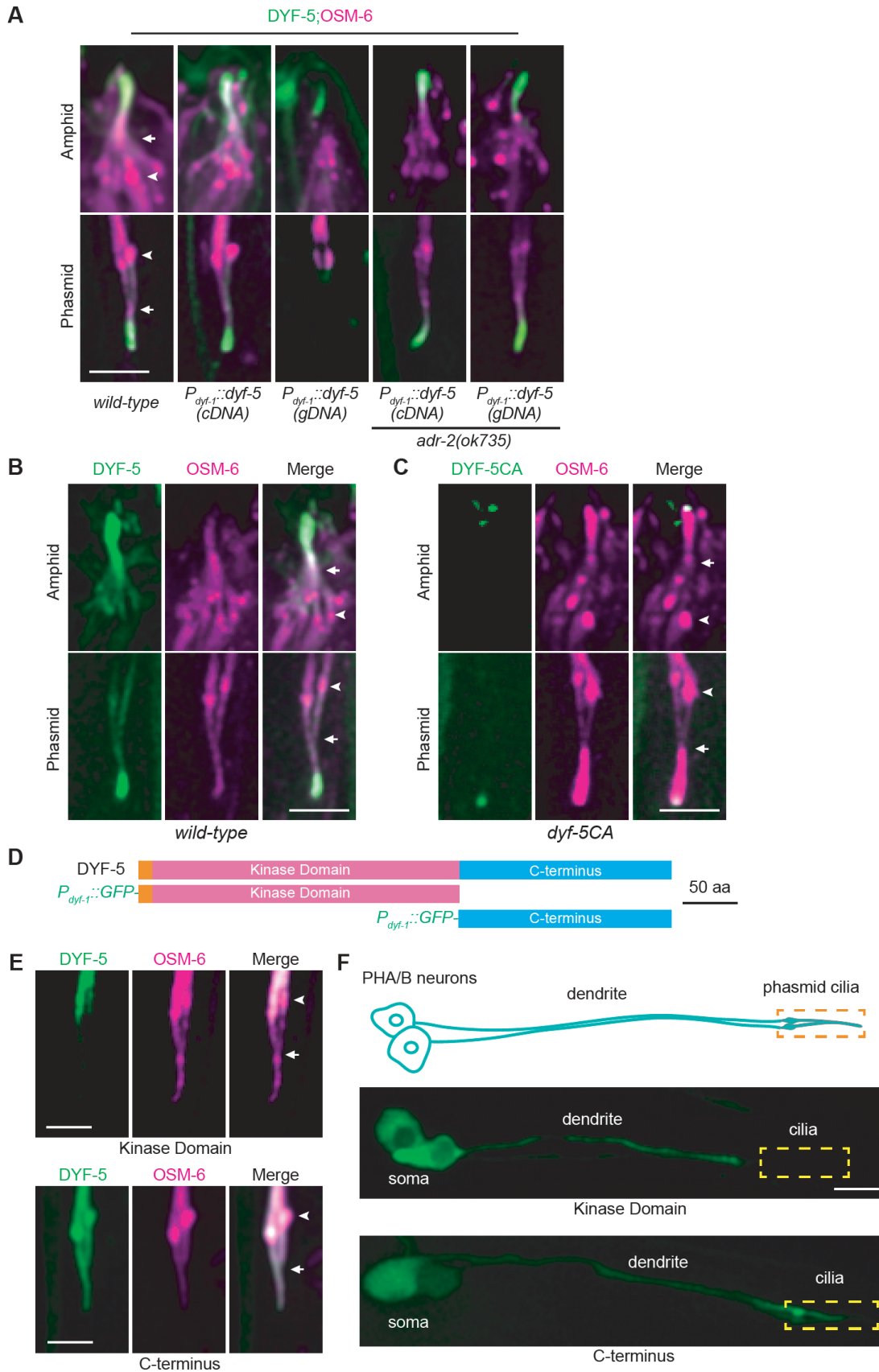


Fig. S8. DYF-5 protein localization and the ciliary defects in *dyf-5* animals.

(A-C) Localization of the endogenous GFP::DYF-5 in the indicated strains. GFP was tagged to the N-terminus of DYF-5. mCherry-tagged IFT52/OSM-6 marks cilia. Scale bars in (A)-(C) and (E)-(F) are 5 μm . (D) Schematic domain structures of GFP-tagged DYF-5 kinase domain or C-terminus under the control of the ciliated neuron-specific *Pdyf-1* promoter. Kinase domain, pink; C-terminal domain, blue. The scale bar represents 50 amino acids. (E) Localization of GFP-tagged DYF-5 kinase domain (upper) or C-terminus (lower) in phasmid cilia. mCherry-tagged IFT52/OSM-6 marks cilia. (F) Schematic diagram of phasmid neurons in *C. elegans*. Anterior is to the left, and the dashed box indicates the phasmid cilia (upper). Localization of GFP-tagged DYF-5 kinase domain (middle) or C-terminus (lower) in sensory neurons.

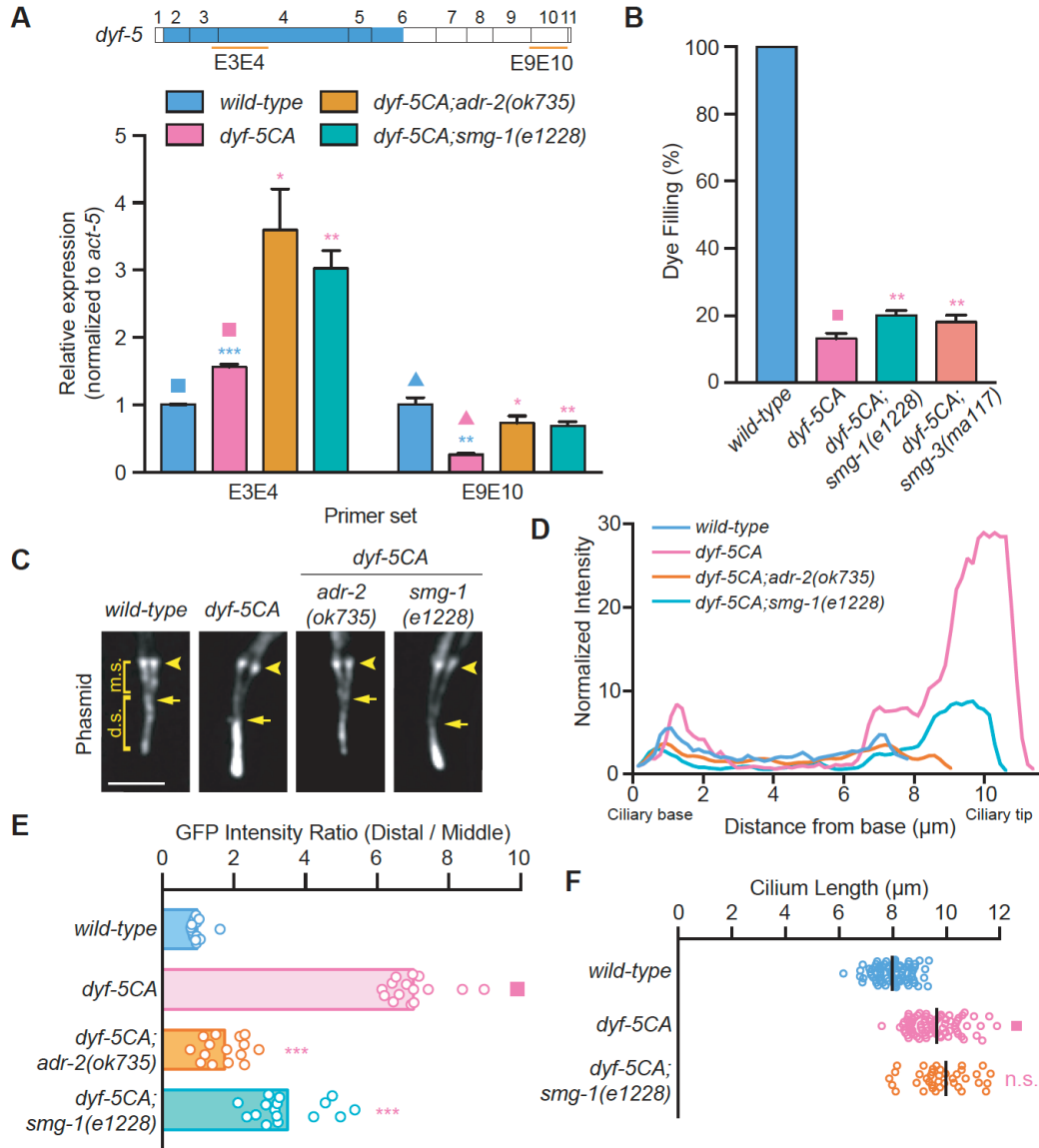


Fig. S9. NMD of the *dyf-5CA* mRNA.

(A) RT-qPCR analysis of relative expression of the *dyf-5* mRNA in *wild-type* and mutant animals. N = 3 biological replicates for each genotype. Primer sets used are indicated above the graph. Bar graphs and error bars represent mean \pm SEM. (B) Percentage of dye-filling positive in the indicated strains. N = 100 – 200. Mean \pm SD (error bars). (C–D) Representative images (C) and fluorescence intensity quantifications (D) of GFP-tagged IFT52/OSM-6 along phasmid cilia with different genotypes. The scale bar is 5 μm . (E) Fluorescence ratio of GFP-tagged IFT52/OSM-6 between the distal and the middle phasmid ciliary segments in different genotypes. The high fluorescence in the distal ciliary portions of *dyf-5CA* animals indicates the aggregation of IFT-particles marked by IFT52/OSM-6::GFP, whereas mutations of *adr-2* or *smg-1* reduced the aggregations. N = 15 for each genotype. (F) Cilium length of phasmid sensory cilia in the indicated strains. Cilium length was measured using the IFT52/OSM-6::GFP fluorescence, N = 30 – 60. Statistical significance compared with the control with a matching color code is based on Student's t-test, n.s., not significant, * $p < 0.05$, ** $p < 0.01$, *** $p < 0.001$.

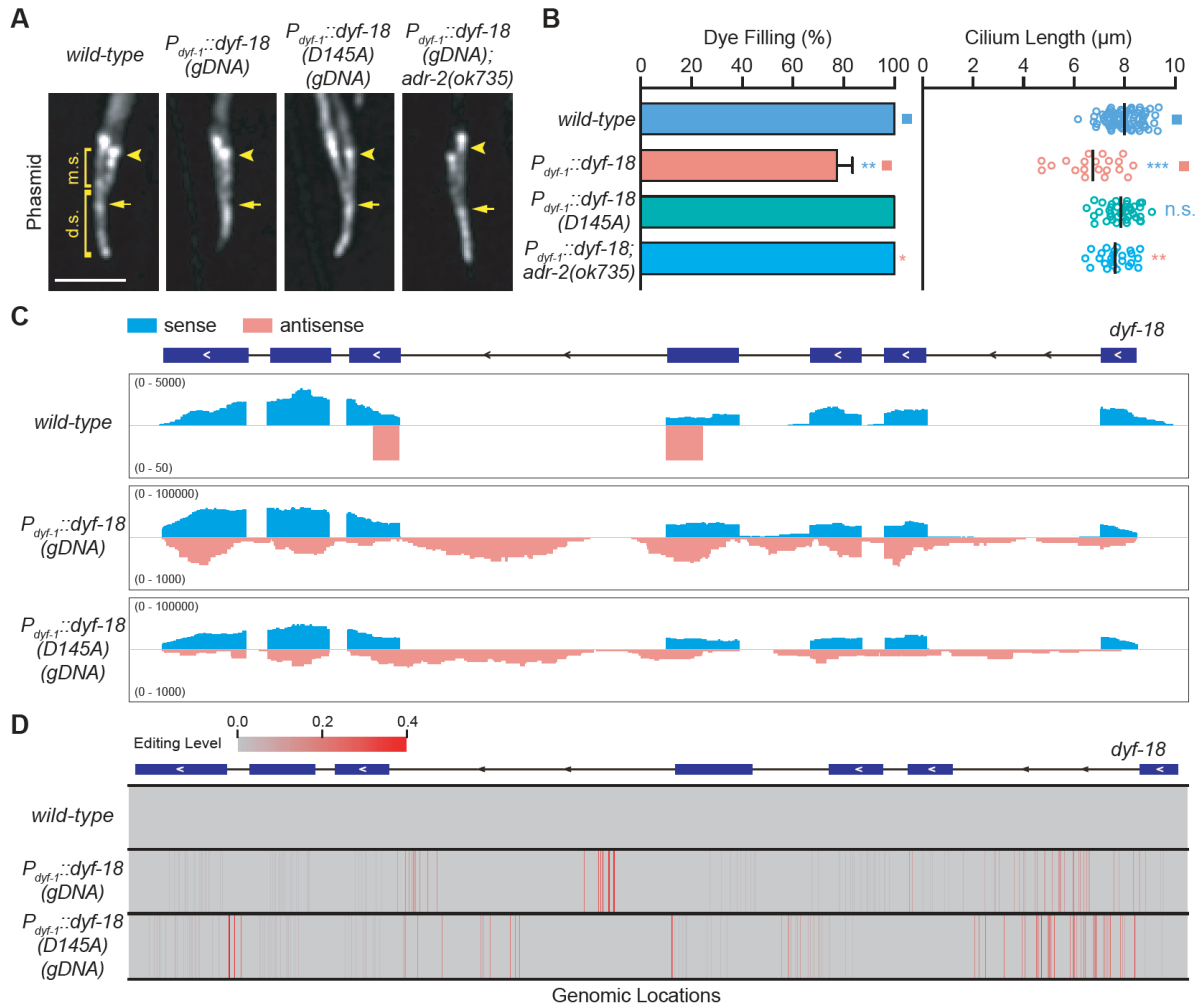


Fig. S10. Overexpression of *dyf-18* caused ciliary defects.

(A) Phasmid ciliary phenotypes in the indicated strains visualized using GFP-tagged IFT52/OSM-6. The scale bar is 5 μm . (B) Percentage of dye-filling (mean \pm SD) positive animals in the indicated strains. $N = 100 - 200$ (left). Cilium length of phasmid cilia in the indicated strains (right), $N = 30 - 60$. Statistical significance compared with the control with a matching color code is based on Student's t-test, n.s., not significant, $*p < 0.05$, $**p < 0.01$, $***p < 0.001$. (C) The mapping profiles of sense and antisense RNA at the *dyf-18* locus in the wild type *dyf-18* (upper) or kinase-dead *dyf-18(D145A)* (lower) genomic DNA (gDNA) overexpressed animals (sense reads, blue; antisense reads, pink). (D) RNA editing clusters at the *dyf-18* locus in the wild type *dyf-18* (upper) or kinase-dead *dyf-18(D145A)* (lower) genomic DNA (gDNA) overexpression animals. The bar for editing level is shown on the top.

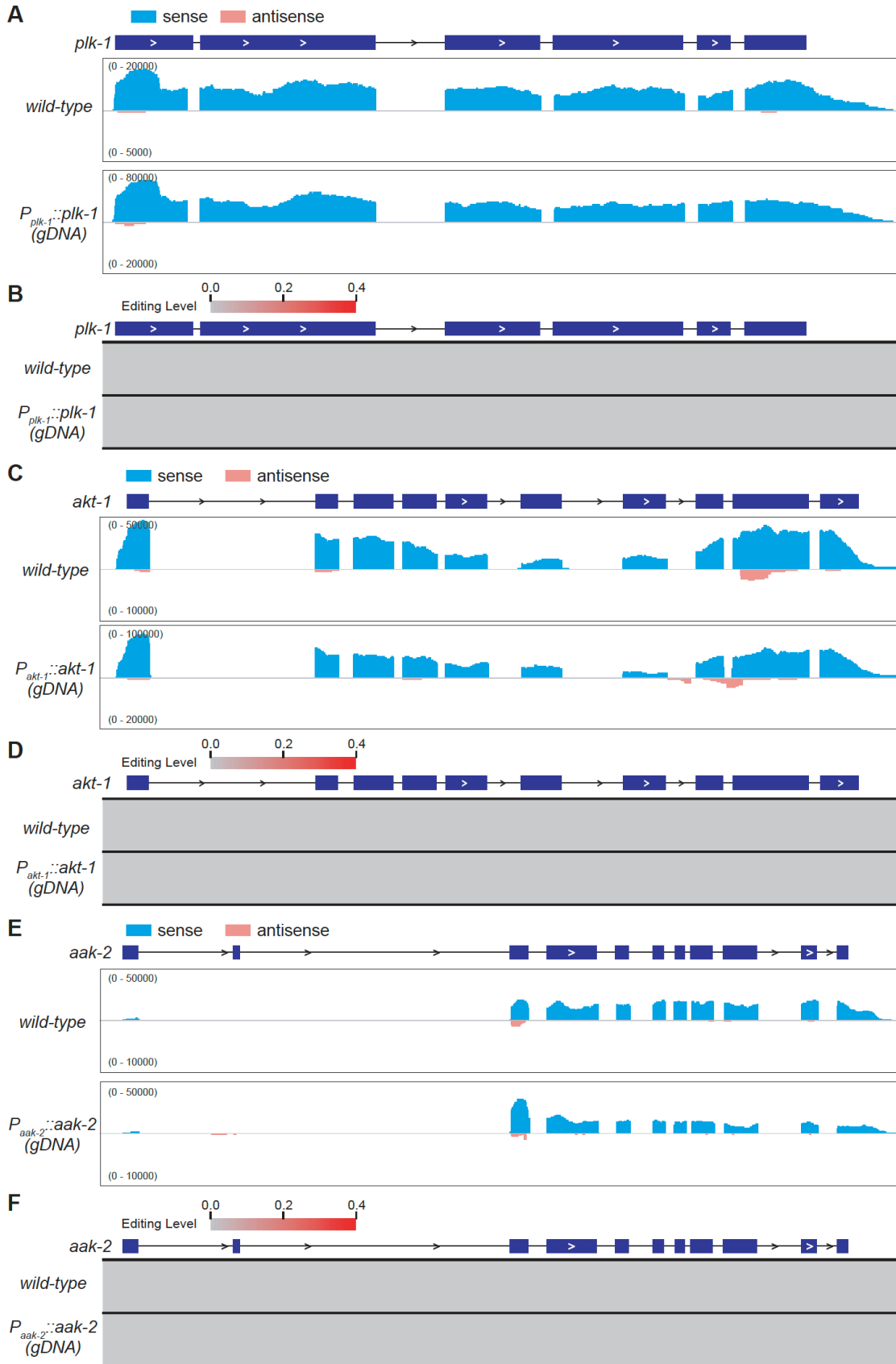


Fig. S11. Antisense RNA and RNA editing in the *plk-1*, *akt-1*, and *aak-2* genomic DNA (gDNA) overexpression animals.

(A, C, E) The mapping profiles of sense and antisense RNA at the *plk-1*, *akt-1*, and *aak-2* locus in the *plk-1*, *akt-1*, and *aak-2* genomic DNA (gDNA) overexpression animals (sense reads, blue; antisense reads, pink). (B, D, F) RNA editing clusters at the *plk-1*, *akt-1*, and *aak-2* locus in the *plk-1*, *akt-1*, and *aak-2* genomic DNA (gDNA) overexpression animals, and the bar for editing level is shown on the top.

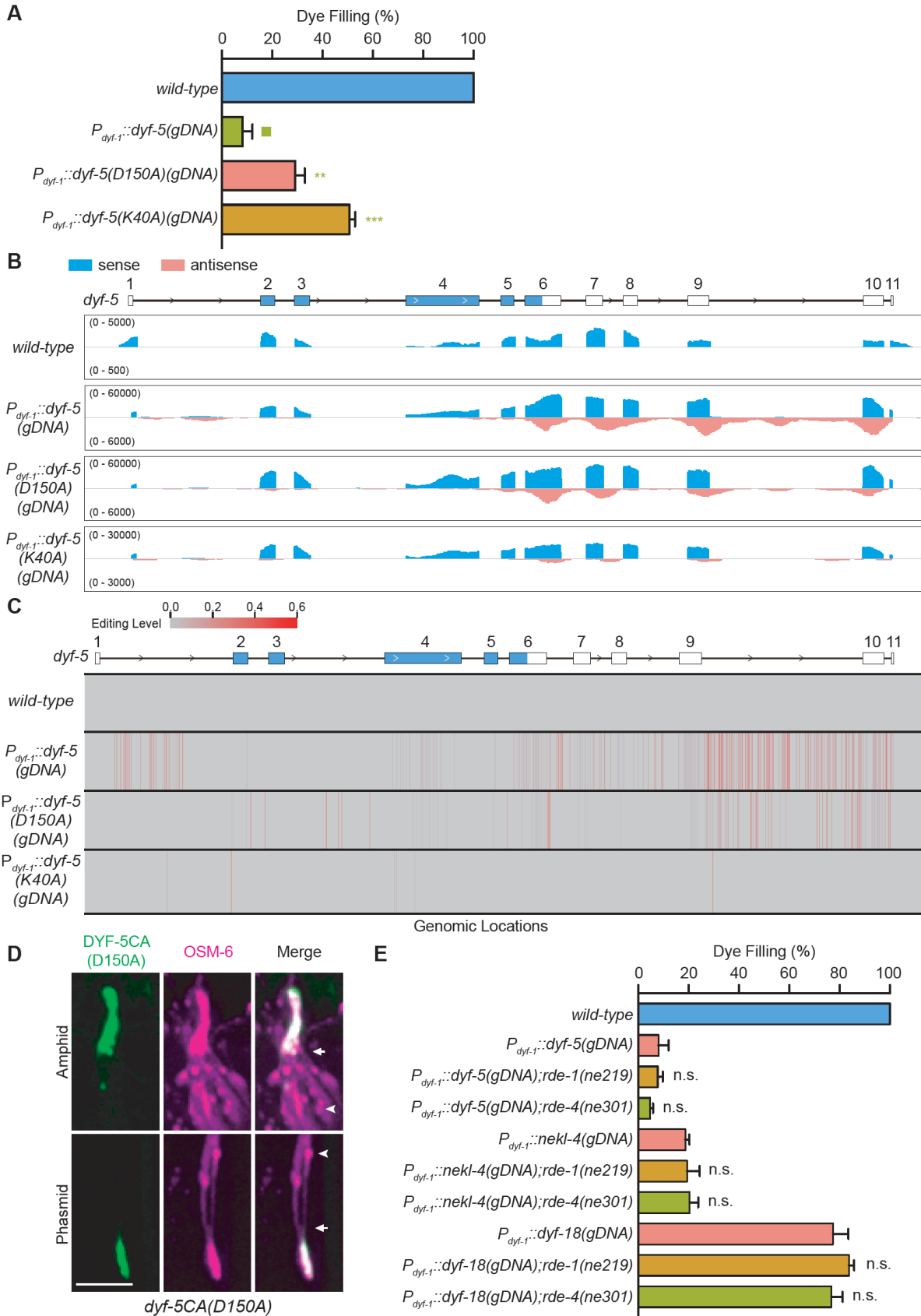


Fig. S12. Kinase hyperactivation causes aberrant antisense transcription and RNA editing at *dyf-5* and ciliary defects.

(A) Percentage of dye-filling (mean \pm SD) positive animals in the indicated strains. N = 100 – 200. (B) The mapping profiles of sense and antisense RNA at the *dyf-5* locus in the wild type *dyf-5* (upper) or kinase-dead *dyf-5(D150A)* and *dyf-5(K40A)* (lower) genomic DNA (gDNA) overexpression animals (sense reads, blue; antisense reads, pink). (C) RNA editing clusters at the *dyf-5* locus in the wild type *dyf-5* (upper) or kinase-dead *dyf-5(D150A)* and *dyf-5(K40A)* (lower) genomic DNA (gDNA) overexpression animals, and the bar for editing level is shown on the top. (D) Localization of the endogenous GFP::DYF-5CA(D150A) in amphid and phasmid cilia. GFP was tagged to the N-terminus of DYF-5. mCherry-tagged IFT52/OSM-6 marks cilia. The scale bar is 5 μ m. (E) Percentage of dye-filling in *wild-type* and *rde-1* or *rde-4* mutant animals that overexpressed kinase genomic DNAs. N = 200 – 300. Mean \pm SD (error bars). Statistical significance compared with the control is based on Student's t-test, n.s., not significant, * $p < 0.05$, ** $p < 0.01$, *** $p < 0.001$.

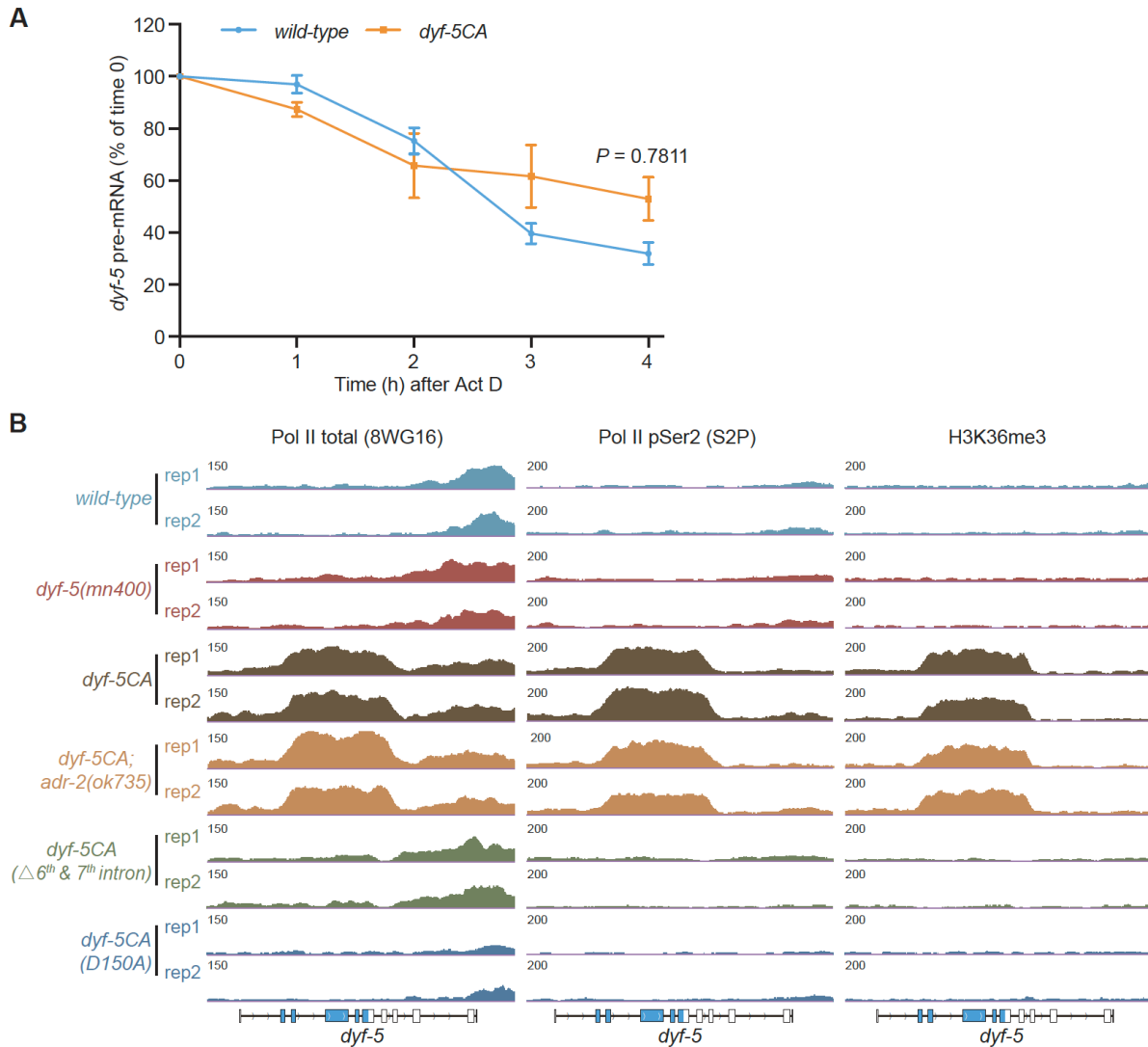


Fig. S13. Transcription regulation of the *dyf-5CA* mRNA.

(A) Worms were treated with Actinomycin D (200 μ g/ml). The *dyf-5* pre-mRNA levels that remained after treatment were examined at the indicated time points. P values for comparison between *wild-type* and *dyf-5CA* were shown. Data represent the mean \pm s.d. of three biologically independent experiments (two-tailed Student's t-test). (B) IGV visualization of Pol II total (8WG16) (left), Pol II pSer2 (S2P) (middle) and H3K36me3 (right) ChIP-seq at the *dyf-5* loci. 8WG16, hypophosphorylated Pol II. S2P, elongating Pol II.

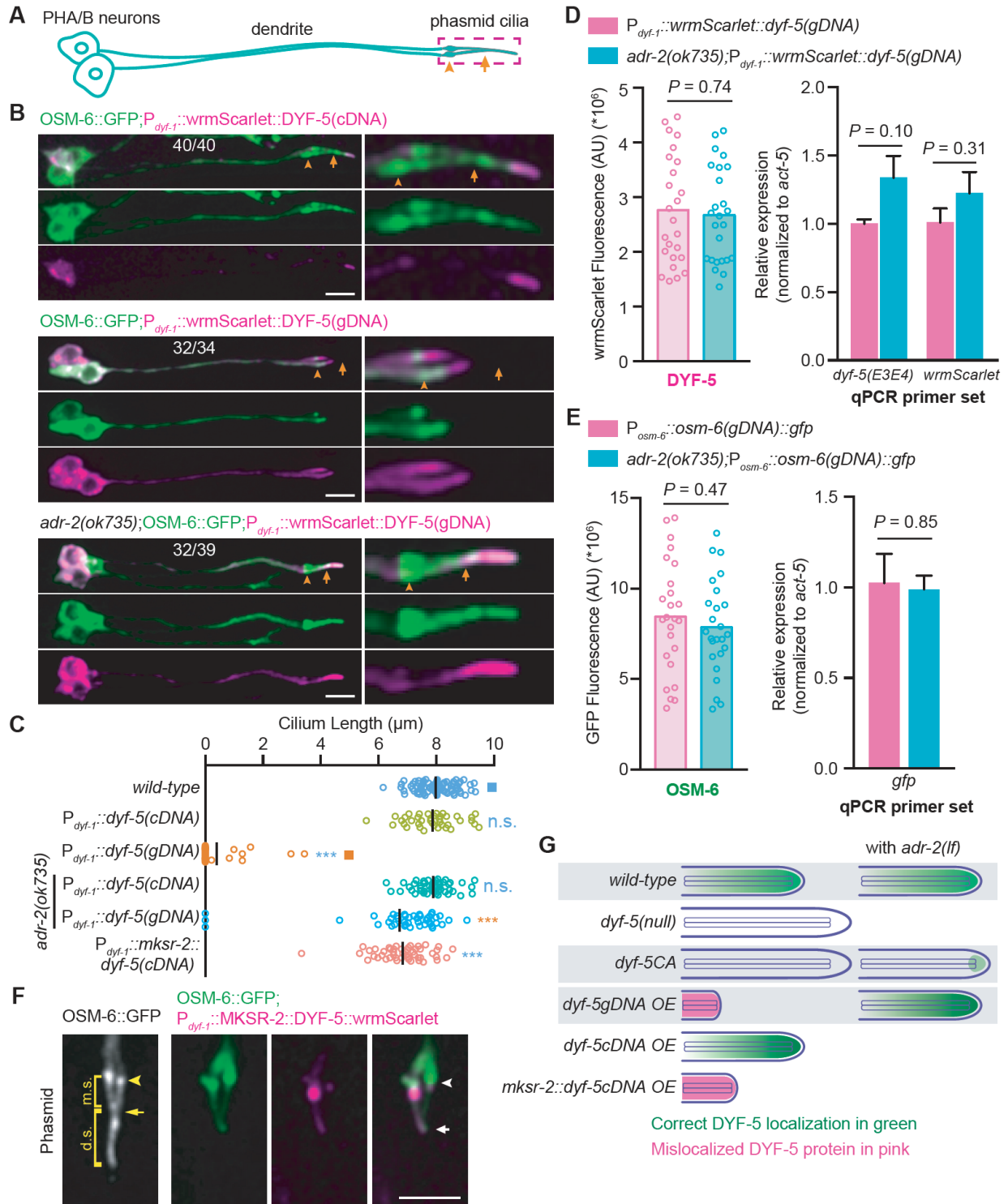


Fig. S14. DYF-5 Localization patterns and the model.

(A) Schematic diagram of the *C. elegans* phasmid neurons. Anterior is to the left, and the dashed box indicates the phasmid cilia. Arrowhead indicates a ciliary base and transition zone, and arrow indicates junction between the middle and distal segment. (B) Localization of DYF-5

proteins from the $P_{dyf-1}::wrmScarlet::DYF-5$ (cDNA) (top) or $P_{dyf-1}::wrmScarlet::DYF-5$ (gDNA) (middle and lower) in sensory neurons. The right panels are the enlarged images of the phasmid cilia. The digits within the images represent the number of phasmid cilia shown and the total observed phasmid cilia. **(C)** Cilium length of phasmid sensory cilia in the indicated strains. Cilium length was measured using the IFT52/OSM-6::GFP fluorescence, $N = 30 - 60$. **(D)** Bar charts represent $wrmScarlet::DYF-5$ fluorescence intensity at the phasmid neurons in the indicated strains. $N = 25$ (left). RT-qPCR analysis of relative expression of the *dyf-5* or *wrmScarlet* mRNA in $P_{dyf-1}::wrmScarlet::dyf-5$ (gDNA) or *adr-2(ok735);P_{dyf-1}::wrmScarlet::dyf-5*(gDNA) animals at the fourth larval stage (L4) (right). The position of the *dyf-5* E3E4 primer set is shown in Figure S9A. All the primer information for qPCR is available in the supplemental Table S4. $N = 3$ biological replicates for each genotype. Bar graphs and error bars represent mean \pm SEM. **(E)** Bar charts represent OSM-6::GFP fluorescence intensity at the phasmid neurons in the indicated strains. $N = 25$ (left). RT-qPCR analysis of relative expression of the *osm-6::gfp* mRNA in $P_{osm-6}::osm-6$ (gDNA)::*gfp* or *adr-2(ok735);P_{osm-6}::osm-6*(gDNA)::*gfp* animals at the fourth larval stage (L4) (right). We use *gfp* relative expression level to represent the *osm-6* mRNA level. $N = 3$ biological replicates for each genotype. Bar graphs and error bars represent mean \pm SEM. **(F)** Localization of the MKSR-2::DYF-5 protein around the ciliary base from the $P_{dyf-1}::MKSR-2::DYF-5$ (cDNA)::*wrmScarlet* animals. GFP-tagged IFT52/OSM-6 marks cilia. Scale bars in **(B)** and **(F)** are 5 μ m. **(G)** A model summarizes DYF-5 localization in different strains. Statistical significance compared with the control with a matching color code is based on Student's t-test, n.s., not significant, * $p < 0.05$, ** $p < 0.01$, *** $p < 0.001$.

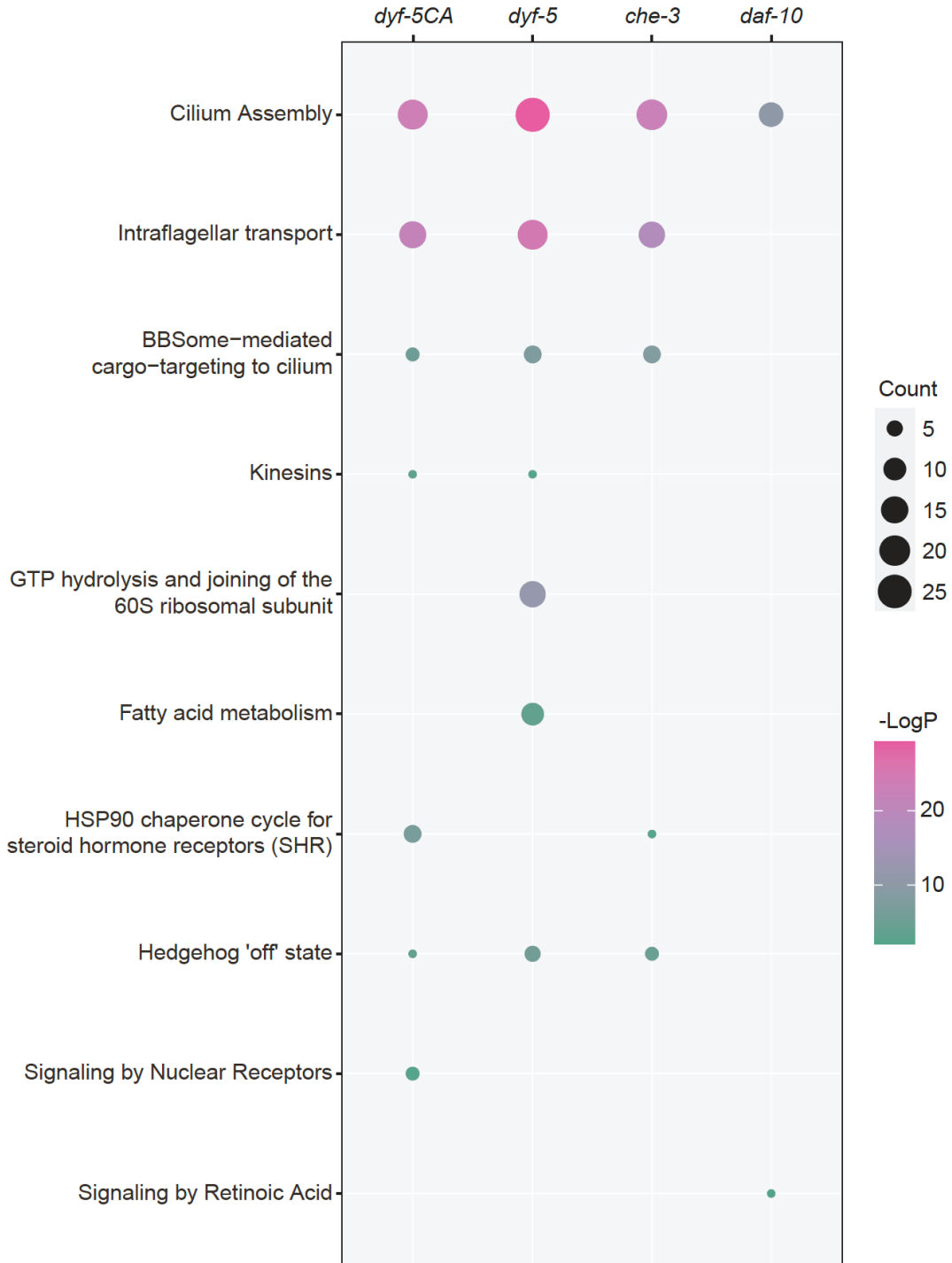


Fig. S15. Dotplot visualization of gene enrichment analysis for the up-regulated genes in *dyf-5CA*, *dyf-5(mn400)*, *che-3(gk116178)*, and *daf-10(e1387)*. Gene enrichment analyses were performed using Metascape against the GO dataset for Reactome Gene Sets. The color of the dots represents the LogP value for each enriched GO term, and its size represents the number of genes enriched in the reactome gene set.

Table S1. *C. elegans* Strains in this study

Strain Name	Genotype	Method
N2	<i>wild-type</i>	N.A.
GOU4500	<i>cas501(dyf-5(T164E)) I.</i>	Microinjection
SP1745	<i>dyf-5(mn400) I.</i>	<i>Caenorhabditis Genetics Center</i>
SP2101	<i>ncl-1(e1865) unc-36(e251); osm-6(p811); mnIs17[P_{osm-6}::osm-6::GFP unc-36(+)].</i>	<i>Caenorhabditis Genetics Center</i>
GOU1513	<i>dyf-5(mn400) I; mnIs17 V.</i>	Genetic cross
GOU1983	<i>dyf-5(cas501) I; mnIs17 V.</i>	Genetic cross
GOU2154	<i>casIs550[OSM-6::mCherry].</i>	Microinjection
GOU1810	<i>casIs586[KAP-1::GFP].</i>	Microinjection
GOU4514	<i>cas1057[gfp::dyf-5 knock-in] I.</i>	Microinjection
GOU4515	<i>cas1058[gfp::dyf-5(T164E) knock-in] I.</i>	Microinjection
GOU3633	<i>cas1057 I; casIS550.</i>	Genetic cross
GOU3634	<i>cas1058 I; casIS550</i>	Genetic cross
GOU4516	<i>casEX5047[cas1057 I; P_{dyf-1}::dyf-5-cDNA].</i>	Microinjection
GOU3820	<i>dyf-5(cas501) I; mnIs17 V; P_{dyf-1}::dyf-5-cDNA.</i>	Microinjection
GOU3821	<i>dyf-5(cas501) I; mnIs17 V; P_{dyf-1}::dyf-5(T164E)-cDNA.</i>	Microinjection
GOU4517	<i>casEX5049[cas1057 I; casIs550; P_{dyf-1}::dyf-5(T164E)-cDNA].</i>	Microinjection
GOU3857	<i>cas1058cas890(gfp::dyf-5CA(D150A)) I; casIS550.</i>	Microinjection
GOU3811	<i>casIS586; casIS550.</i>	Genetic cross
GOU3809	<i>dyf-5(cas501) I; casIS586; casIS550.</i>	Genetic cross
GOU3812	<i>dyf-5(mn400) I; casIS586; casIS550.</i>	Genetic cross
GOU4501	<i>cas1009(adr-2(T277I)) III.</i>	Genetic cross
GOU4502	<i>cas1010(adr-2(Q476*)) III.</i>	Genetic cross
GOU4503	<i>cas1011(adr-2(G319E)) III.</i>	Genetic cross
GOU4504	<i>cas1012(adr-2(S169F)) III.</i>	Genetic cross
GOU4505	<i>cas506(dyf-5(cas501) I; adr-2(cas1009) III).</i>	EMS Screen
GOU4506	<i>cas517(dyf-5(cas501) I; adr-2(cas1010) III).</i>	EMS Screen
GOU4507	<i>cas518(dyf-5(cas501) I; adr-2(cas1011) III).</i>	EMS Screen
GOU4508	<i>cas519(dyf-5(cas501) I; adr-2(cas1012) III).</i>	EMS Screen
BB21	<i>adr-1(tm668) I; adr-2(ok735) III.</i>	<i>Caenorhabditis Genetics Center</i>
QD1	<i>adbp-1(qj1) II.</i>	<i>Caenorhabditis Genetics Center</i>
GOU2348	<i>adr-2(ok735) III; mnIs17 V.</i>	Genetic cross
GOU2955	<i>adbp-1(qj1) II; mnIs17 V.</i>	Genetic cross
GOU2354	<i>adr-1(tm668) I; mnIs17 V.</i>	Genetic cross

GOU2387	<i>dyf-5(cas501) I; adr-2(ok735) III; mnIs17 V.</i>	Genetic cross
GOU2953	<i>dyf-5(mn400) I; adr-2(ok735) III; mnIs17 V.</i>	Genetic cross
GOU2393	<i>dyf-5(cas501) I; adr-1(tm668) I; mnIs17 V.</i>	Genetic cross
GOU2422	<i>dyf-5(cas501) I; adbp-1(qj1); mnIs17.</i>	Genetic cross
GOU4509	<i>casEx5067[Pdyf-1::adbp-1::gfp; rol-6(su1006)(+)].</i>	Microinjection
GOU4510	<i>casEx5073[Pdyf-1::adr-2; rol-6(su1006)(+)].</i>	Microinjection
GOU4511	<i>casEx1697[Pdyf-1::adr-2::gfp; Pdyf-1::osm-6::mCherry; rol-6(su1006)(+)].</i>	Microinjection
GOU3863	<i>dyf-5(cas501) I; adr-2(ok735) III; casEx1697.</i>	Genetic cross
GOU3848	<i>cas501cas1130[dyf-5-T164E & 6th intron deletion] I.</i>	Microinjection
GOU4512	<i>cas501cas1110[dyf-5-T164E & 7th intron deletion] I.</i>	Microinjection
GOU4513	<i>cas501cas1079[dyf-5(T164E); dyf-5-6th,7th-intron-deletion] I.</i>	Microinjection
GOU3849	<i>cas501cas1131[dyf-5-T164E & 6th and 7th intron edited a substituted by t] I.</i>	Microinjection
GOU3860	<i>cas501cas1130 I; mnIs17 V.</i>	Genetic cross
GOU3822	<i>cas501cas1110 I; mnIs17 V.</i>	Genetic cross
GOU3769	<i>cas501cas1079 I; mnIs17 V.</i>	Genetic cross
GOU3861	<i>cas501cas1131 I; mnIs17 V.</i>	Genetic cross
GOU4560	<i>cas501cas1200[dyf-5-T164E & 8th intron deletion] I.</i>	Microinjection
GOU4570	<i>cas501cas1200[dyf-5-T164E & 8th intron deletion] I; mnIs17 V.</i>	Genetic cross
GOU3765	<i>cas1058 I; adr-2(ok735) III; casIS550</i>	Genetic cross
GOU3768	<i>cas1057 I; adr-2(ok735) III; casIS550.</i>	Genetic cross
GOU3847	<i>cas1057cas891[gfp::dyf-5b::wrmScarlet knock-in] I.</i>	Microinjection
GOU3850	<i>cas1058cas891[gfp::dyf-5b(T164E)::wrmScarlet knock-in] I.</i>	Microinjection
GOU3856	<i>cas1057cas891 I; cas498 X.</i>	Genetic cross
GOU3862	<i>cas1058cas891 I; cas498 X.</i>	Genetic cross
GOU4170	<i>cas1057cas891 I; cas498 X; adr-2(ok735) III.</i>	Genetic cross
GOU4171	<i>cas1058cas891 I; cas498 X; adr-2(ok735) III.</i>	Genetic cross
GOU4520	<i>casEx5048[cas1057 I; casIS550; Pdyf-1::dyf-5-gDNA].</i>	Genetic cross
GOU4521	<i>casEx5060[Pdyf-1::dyf-5-gDNA].</i>	Microinjection
GOU4523	<i>casEx5057[Pdyf-1::dyf-5-gDNA(no 8th intron)].</i>	Microinjection
GOU4524	<i>casEx5058[Pdyf-1::dyf-5-gDNA(no 7th intron)].</i>	Microinjection
GOU4525	<i>casEx5059[Pdyf-1::dyf-5-gDNA(no 6th intron)].</i>	Microinjection
GOU4527	<i>casEx5063[Pdyf-1::dyf-5-cDNA(add 6th intron)].</i>	Microinjection
GOU4528	<i>casEx5064[Pdyf-1::dyf-5-cDNA(add 7th intron)].</i>	Microinjection
GOU4529	<i>casEx5065[cas1057 I; casIS550; Pdyf-1::dyf-5-cDNA(add 8th intron)].</i>	Microinjection

GOU4530	<i>casEx5066[cas1057 I; casIS550; Pdyf-1::dyf-5-cDNA(add 6th,7th and 8th intron)].</i>	Microinjection
GOU4532	<i>casEx5061[Pdyf-1::gfp::dyf-5-C terminus].</i>	Microinjection
GOU4533	<i>casEx5062[Pdyf-1::gfp::dyf-5-kinase domain].</i>	Microinjection
GOU3851	<i>casEx5062; casIS550.</i>	Genetic cross
GOU3852	<i>casEx5061; casIS550.</i>	Genetic cross
GOU3806	<i>cas1057 I; casIS550; Pdyf-1::dyf-5-cDNA.</i>	Genetic cross
GOU3817	<i>casEx5048; adr-2(ok735) III.</i>	Genetic cross
GOU3818	<i>cas1057 I; casIS550; adr-2(ok735) III; Pdyf-1::dyf-5-cDNA.</i>	Genetic cross
WM27	<i>rde-1(ne219) V.</i>	<i>Caenorhabditis Genetics Center</i>
GOU2979	<i>dyf-5(cas501) I; rde-1(ne219) V; mnIS17 V.</i>	Genetic cross
GOU2983	<i>dyf-5(cas501) I; rrf-3(pk1426) II; mnIS17 V.</i>	Genetic cross
GOU2980	<i>dyf-5(cas501) I; rrf-3(pk1426) II; adr-2(ok735) III; mnIS17 V.</i>	Genetic cross
GOU3834	<i>dyf-5(cas501) I; adr-2(ok735) III; rde-1(ne219) V.</i>	Genetic cross
GOU3593	<i>dyf-5(cas501) I; smg-1(e1228) I.</i>	Genetic cross
GOU3589	<i>dyf-5(cas501) I; smg-3(ma117) IV.</i>	Genetic cross
GOU4580	<i>casEx5075[Pdyf-1::nekl-4-gDNA].</i>	Microinjection
GOU4581	<i>casEx5046[Pdyf-1::dyf-18-gDNA].</i>	Microinjection
GOU4582	<i>casEx5075[Pdyf-1::nekl-4-gDNA]; mnIS17.</i>	Genetic cross
GOU4583	<i>casEx5046[Pdyf-1::dyf-18-gDNA]; mnIS17.</i>	Genetic cross
GOU4584	<i>casEx5075[Pdyf-1::nekl-4-gDNA]; adr-2(ok735); mnIS17.</i>	Genetic cross
GOU4585	<i>casEx5046[Pdyf-1::dyf-18-gDNA]; adr-2(ok735); mnIS17.</i>	Genetic cross
GOU4660	<i>casEx5085[Pdyf-1::nekl-4(D609A)-gDNA].</i>	Microinjection
GOU4661	<i>casEx5085[Pdyf-1::nekl-4(D609A)-gDNA]; mnIS17.</i>	Genetic cross
GOU4662	<i>casEx5084[Pdyf-1::dyf-18(D145A)-gDNA].</i>	Microinjection
GOU4663	<i>casEx5084[Pdyf-1::dyf-18(D145A)-gDNA]; mnIS17.</i>	Genetic cross
GOU4664	<i>casEX5079[Pplk-1::plk-1-gDNA;rol-6(su1006)(+)].</i>	Microinjection
GOU4665	<i>casEX5076[Pakt-1::akt-1-gDNA;rol-6(su1006)(+)].</i>	Microinjection
GOU4666	<i>casEX5078[Paak-2::aak-2-gDNA; rol-6(su1006)(+)].</i>	Microinjection
GOU4667	<i>casEX5077[Pakt-2::akt-2-gDNA; rol-6(su1006)(+)].</i>	Microinjection
GOU4625	<i>cas1057 I; casIS550; Pdyf-1::dyf-5(K40A)-genomic DNA; rol-6(su1006)(+).</i>	Microinjection
GOU4668	<i>cas1057 I; casIS550; Pdyf-1::dyf-5(D150A)-genomic DNA; rol-6(su1006)(+).</i>	Microinjection
WM49	<i>rde-4(ne301) III.</i>	<i>Caenorhabditis Genetics Center</i>
GOU4612	<i>cas1057 I; casIS550; Pdyf-1::dyf-5-genomic DNA; rol-6(su1006)(+); rde-1(ne219).</i>	Genetic cross

GOU4613	<i>cas1057 I; casIS550; Pdyf-1::dyf-5-genomic DNA; rol-6(su1006)(+); rde-4(ne301).</i>	Genetic cross
GOU4618	<i>Pdyf-1::nekl-4-genomic DNA; rol-6(su1006)(+); rde-1(ne219); mnIS17.</i>	Genetic cross
GOU4619	<i>Pdyf-1::nekl-4-genomic DNA; rol-6(su1006)(+); rde-4(ne301); mnIS17.</i>	Genetic cross
GOU4616	<i>Pdyf-1::dyf-18-genomic DNA; rol-6(su1006)(+); rde-1(ne219); mnIS17.</i>	Genetic cross
GOU4617	<i>Pdyf-1::dyf-18-genomic DNA; rol-6(su1006)(+); rde-4(ne301); mnIS17.</i>	Genetic cross
GOU4669	<i>casEX5086[cas1057 I; Pdyf-1::wrmScarlet-dyf-5-cDNA].</i>	Microinjection
GOU4670	<i>casEX5087[cas1057 I; Pdyf-1::wrmScarlet-dyf-5-genomic DNA.</i>	Microinjection
GOU4620	<i>Pdyf-1::mksr-2::dyf-5(cDNA)::wrmScarlet; mnIS17.</i>	Microinjection
VC20081	<i>che-3(gk116178) I.</i>	<i>Caenorhabditis Genetics Center</i>
PR802	<i>osm-3(p802) IV.</i>	<i>Caenorhabditis Genetics Center</i>
CB1387	<i>daf-10(e1387) IV.</i>	<i>Caenorhabditis Genetics Center</i>

Table S2. CRISPR-Cas9 Targets in this study

Gene	CRISPR-Cas9 targets (PAM)	Application Description
<i>dyf-5</i>	Sg1: CCA TATACAGATTATGTATCAAC	Genomic editing <i>dyf-5</i> (T164E) and <i>dyf-5</i> (D150A)
	Sg2: AGGGCAAGAAGCCATGTCAT CGG	N-terminal GFP Knock-in
	Sg3: CCA TGTCATCGGCTGTAAACTT	N-terminal GFP Knock-in
	Sg4: CCA CATTGCTTTCCAGGTTGTGA	Genomic editing <i>dyf-5</i> ($\Delta 6^{\text{th}}$ intron), <i>dyf-5</i> ($\Delta 7^{\text{th}}$ intron), <i>dyf-5</i> ($\Delta 6^{\text{th}}$ and 7^{th} intron) and <i>dyf-5</i> (substitution of 6^{th} and 7^{th} intron)
	Sg5: AGATCAGATAACAAGCCTCT GGG	Genomic editing <i>dyf-5</i> ($\Delta 6^{\text{th}}$ intron), <i>dyf-5</i> ($\Delta 7^{\text{th}}$ intron), <i>dyf-5</i> ($\Delta 6^{\text{th}}$ and 7^{th} intron), <i>dyf-5</i> (substitution of 6^{th} and 7^{th} intron), and <i>dyf-5</i> ($\Delta 8^{\text{th}}$ intron)
	Sg6: TAATACGGGTCGAGTCGATT GGG	C-terminal wrmScarlet Knock-in
	Sg7: CCA TCGTTCGAAATATTGCATAA	C-terminal wrmScarlet Knock-in

Table S3. Plasmids and Primers in this study

Plasmid Name	Forward Primer	Reverse Primer	Notes
pDD162-Peft-3::Cas9 + PU6::dyf-5 sg1	TACATAATCTGT ATAGTTTTAGAG CTAGAAATAGCA AG	TATACAGATTA TGTATCAACCA AGACATCTCGC AATAGG	PCR from pDD162-Peft-3::Cas9+PU6::Empty sgRNA
pDD162-Peft-3::Cas9 + PU6::dyf-5 sg2	AAGAAGCCATGT CATGTTTTAGAG CTAGAAATAGCA AG	ATGACATGGCT TCTTGCCCTCA AGACATCTCGC AATAGG	PCR from pDD162-Peft-3::Cas9+PU6::Empty sgRNA
pDD162-Peft-3::Cas9 + PU6::dyf-5 sg3	TAACAGCCGATG ACAGTTTTAGAG CTAGAAATAGCA AG	TGTCATCGGCT GTTAAACTTCA AGACATCTCGC AATAGG	PCR from pDD162-Peft-3::Cas9+PU6::Empty sgRNA
pDD162-Peft-3::Cas9 + PU6::dyf-5 sg4	ACCTGGAAAAGCA ATGGTTTTAGAG CTAGAAATAGCA AG	CATTGCTTTCC AGGTTGTGACA AGACATCTCGC AATAGG	PCR from pDD162-Peft-3::Cas9+PU6::Empty sgRNA
pDD162-Peft-3::Cas9 + PU6::dyf-5 sg5	AGATAACAAGCC TCTGTTTTAGAG CTAGAAATAGCA AG	AGAGGCTTGTT ATCTGATCTCA AGACATCTCGC AATAGG	PCR from pDD162-Peft-3::Cas9+PU6::Empty sgRNA
pDD162-Peft-3::Cas9 + PU6::dyf-5 sg6	CGGGTCGAGTCG ATTGTTTTAGAG CTAGAAATAGCA AG	AATCGACTCGA CCCGTATTACA AGACATCTCGC AATAGG	PCR from pDD162-Peft-3::Cas9+PU6::Empty sgRNA
pDD162-Peft-3::Cas9 + PU6::dyf-5 sg7	CAATATTTGAA CGAGTTTTAGAG CTAGAAATAGCA AG	TCGTTGAAAT ATTGCATAACA AGACATCTCGC AATAGG	PCR from pDD162-Peft-3::Cas9+PU6::Empty sgRNA
pPD95.77-dyf-5(T164E) genomic template for Knock-in	GTACCGGTAGAA AAAGACACTGGT GATCGAGTTGCA ATT	GAAACGCGCG AGACGCAGAG GCTTGTTATCT GATCTGAA	dyf-5 genomic fragment was amplified from N2 and cloned into pPD95.77 via In-Fusion Advantage PCR Cloning Kit
pPD95.77-dyf-5(T164E) template for Knock-in	TATGAGGATTAT GTATCAAC	TACATAATCCT CATATGGTG	PCR from pPD95.77-dyf-5(T164E) genomic template to modify T164E via In-Fusion Advantage PCR Cloning Kit
pPD95.77-dyf-5(T164E) & D150A) template for Knock-in	ATTGCAGCATT GGATTGGCACGA GAAATCAGATCA	TCCGAATGCTG CAATTTTACA AGTTCTGTTCC ATT	PCR from pPD95.77-dyf-5(T164E) template to modify T164E via In-Fusion Advantage PCR Cloning Kit
pPD95.77-dyf-5 genomic template	GTACCGGTAGAA AAAGAGGGTTG GGGAGGGATAG TG	GAAGAGTAATT GGACGCTGGCC GATCTTTTCCC ATT	dyf-5 genomic fragment was amplified from N2 and cloned into pPD95.77 via In-Fusion Advantage PCR Cloning Kit
pPD95.77-dyf-5(T164E) genomic template	TATGAGGATTAT GTATCAAC	TACATAATCCT CATATGGTG	PCR from pPD95.77-dyf-5 genomic template to modify T164E via In-Fusion Advantage PCR Cloning Kit

pPD95.77- <i>dyf-5</i> genomic template for GFP Knock-in	GTACCGGTAGAA AAAGAGGGTTG GGGAGGGATAG TG	GAAGAGTAATT GGACCCGAATG TTCGACTCTTT CCGTAG	<i>dyf-5</i> genomic fragment was amplified from pPD95.77- <i>dyf-5</i> genomic template and cloned into pPD95.77 via In-Fusion Advantage PCR Cloning Kit
pPD95.77- <i>gfp::dyf-5</i> template for GFP Knock-in	ATGAGTAAAGG AGAAGAAC	ACCGCTACCAC TTCCAGCTTTG TATAGTTCATC CATG	<i>gfp</i> coding sequencing was amplified and cloned into pPD95.77- <i>dyf-5</i> genomic template for GFP Knock-in via In-Fusion Advantage PCR Cloning Kit
pPD95.77- <i>dyf-5(T164E)(Δ6th intron)</i> template for Knock-in	GCTAAGGCGGCA AAGAAAGATTAC ATTGGATCAGAA AAT	CTTTGCCGCCT TAGCTGTCATT GC	PCR from pPD95.77- <i>dyf-5(T164E)</i> genomic template to modify T164E via In-Fusion Advantage PCR Cloning Kit
pPD95.77- <i>dyf-5(T164E)(Δ7th intron)</i> template for Knock-in	AACTCTTTTTGA AAAATCAGATAA CAAGCCTCTGGG ACC	TTTTCAAAAAG AGTTTCCTTAT TG	PCR from pPD95.77- <i>dyf-5(T164E)</i> genomic template to modify T164E via In-Fusion Advantage PCR Cloning Kit
pPD95.77- <i>dyf-5(T164E)(Δ6th and 7th intron)</i> template for Knock-in	GGTTGTGAACAC AATAAGTAAAG AAGGAATGAAA TT	GGCTTGTTATC TGATTTTTCAA AAAGAGTTTCC TTA	Fragment was amplified from N2 cDNA template and cloned into pPD95.77- <i>dyf-5(T164E)(Δ6th intron)</i> template for Knock-in via In-Fusion Advantage PCR Cloning Kit
pPD95.77- <i>dyf-5(T164E)(subst itution of 6th and 7th intron)</i> template for Knock-in	GCTAAGGCGGCA AAGGTTGGTTAT CACTAATTTTT	CTTTGCCGCCT TAGCTGTCA	PCR from synthesized fragment and cloned into pPD95.77- <i>dyf-5(T164E)(Δ6th intron)</i> template for Knock-in via In-Fusion Advantage PCR Cloning Kit
pPD95.77- <i>dyf-5(T164E)(Δ8th intron)</i> template for Knock-in	GCCAAGTATCCA AAGACTC	CTTTGGATACT TGGCCGGGCAC ATATTTGCTTTT TG	PCR from pPD95.77- <i>dyf-5(T164E)</i> genomic template to modify T164E via In-Fusion Advantage PCR Cloning Kit
pPD95.77- <i>dyf-5</i> genomic template for <i>wrmScarlet</i> Knock-in	GTACCGGTAGAA AAACAGGCCAA GTATCCAAAGAC ACT	GAAGAGTAATT GGACCCGGCAT GATCAAGGAGC AG	<i>dyf-5</i> genomic fragment was amplified from pPD95.77- <i>dyf-5</i> genomic template and cloned into pPD95.77 via In-Fusion Advantage PCR Cloning Kit
pPD95.77- <i>dyf-5::wrmScarlet</i> template for <i>wrmScarlet</i> Knock-in	GGAAGTGGTAGC GGTATGGTCAGC AAGGGAGAGGC AG	CTTGTAGAGCT CGTCCAT TCC	<i>wrmScarlet</i> coding sequencing was amplified and cloned into pPD95.77- <i>dyf-5</i> genomic template for GFP Knock-in via In-Fusion Advantage PCR Cloning Kit
pDONR-P <i>dyf-1::dyf-5b-cDNA</i>	TGTAAGCTTGTC AAAATGTCATCG	GAAGAGTAATT GGACCTATTTT	<i>dyf-5b</i> coding sequence was amplified from cDNA and inserted into pDONR plasmid

	GCTGTAAACTT GCT	ACATATTTGGC TGCCCA	via In-Fusion Advantage PCR Cloning Kit.
pDONR-Pdyf-1::dyf-5b-gDNA	ATGTCATCGGCT GTAAACTTGCT	CTATTTTACAT ATCTGAAAGCA TTTC	dyf-5b genomic fragment was amplified from N2 and inserted into pDONR plasmid via In-Fusion Advantage PCR Cloning Kit.
pDONR-Pdyf-1::dyf-5b(T164E)-cDNA	CCATATGAGGAT TATGTATCAACA AGATGGTATAGA GCA	ATAATCCTCAT ATGGTGGTTTT GATCTGATTTT TCGTG	PCR from pDONR-Pdyf-1::dyf-5b-cDNA to modify T164E via In-Fusion Advantage PCR Cloning Kit
pDONR-Pdyf-1::dyf-5b(T164E)-gDNA	CCATATGAGGAT TATGTATCAACA AGATGGTATAGA GCA	ATAATCCTCAT ATGGTGGTTTT GATCTGATTTT TCGTG	PCR from pDONR-Pdyf-1::dyf-5b-gDNA to modify T164E via In-Fusion Advantage PCR Cloning Kit
pDONR-Pdyf-1::dyf-5b-gDNA(ΔATG)	TGTAAGCTTGTC AAATCATCGGCT GTAAACTTGCT	CTATTTTACAT ATCTGAAAGCA TTTC	PCR from pDONR-Pdyf-1::dyf-5b-gDNA via In-Fusion Advantage PCR Cloning Kit
pDONR-Pdyf-1::dyf-5b-gDNA(Δ6 th intron)	GCTAAGGCGGCA AAGAAAGATTAC ATTGGATCAGAA	CTTTGCCGCCT TAGCTGTCAT	PCR from pDONR-Pdyf-1::dyf-5b-gDNA via In-Fusion Advantage PCR Cloning Kit
pDONR-Pdyf-1::dyf-5b-gDNA(Δ7 th intron)	AACTCTTTTTGA AAAATCAGATAA CAAGCCTCTGGG	TTTTCAAAAAG AGTTTCCTTA	PCR from pDONR-Pdyf-1::dyf-5b-gDNA via In-Fusion Advantage PCR Cloning Kit
pDONR-Pdyf-1::dyf-5b-gDNA(Δ8 th intron)	GCAAATATGTGC CCGGCCAAGTAT CCAAAGACACTC	CGGGCACATAT TTGCTTTTTG	PCR from pDONR-Pdyf-1::dyf-5b-gDNA via In-Fusion Advantage PCR Cloning Kit
pDONR-Pdyf-1::dyf-5b-cDNA(add 6 th intron)	GCTAAGGCGGCA AAGTTGGTTAT CACTAATTTTTT T	TCCAATGTAAT CTTTCTGAAAT GTCTACTTTTT ATTGT	PCR from pDONR-Pdyf-1::dyf-5b-gDNA and cloned into pDONR-Pdyf-1::dyf-5b-cDNA via In-Fusion Advantage PCR Cloning Kit
pDONR-Pdyf-1::dyf-5b-cDNA(add 7 th intron)	AACTCTTTTTGA AAAGTAGGTTGC ATATCTGTTCTA CAG	GGCTTGTTATC TGATCTGAAAT TGTAATTTGTG AATGT	PCR from pDONR-Pdyf-1::dyf-5b-gDNA and cloned into pDONR-Pdyf-1::dyf-5b-cDNA via In-Fusion Advantage PCR Cloning Kit
pDONR-Pdyf-1::dyf-5b-cDNA(add 8 th intron)	GTAAGTCAAAA ATAAATTCA	CTGAAAATTGA AAGAAATAGA	PCR from pDONR-Pdyf-1::dyf-5b-gDNA and cloned into pDONR-Pdyf-1::dyf-5b-cDNA via In-Fusion Advantage PCR Cloning Kit
pDONR-Pdyf-1::dyf-5b-cDNA(add 6 th , 7 th and 8 th intron)	GTTGGTTATCAC TAATTTTTTTTGC	CTGAAAATTGA AAGAAATAGA	PCR from pDONR-Pdyf-1::dyf-5b-gDNA and cloned into pDONR-Pdyf-1::dyf-5b-cDNA via In-Fusion Advantage PCR Cloning Kit

pDONR-Pdyf-1::gfp::dyf-5b-gDNA(Kinase Domain)	GCTGGAAGTGGT AGCGGTTATCTG ATGACAAAAAG GCTT	CTAGAAATATT TATAGCGAAGT GA	PCR from pDONR-Pdyf-1::dyf-5b-gDNA and cloned into pDONR via In-Fusion Advantage PCR Cloning Kit
pDONR-Pdyf-1::gfp::dyf-5b-gDNA(C-terminus)	GCTGGAAGTGGT AGCGGTCAAGTT GCTGAAAAGTTG GGT	GAAGAGTAATT GGACCTATTTT ACATATCTGAA AGCA	PCR from pDONR-Pdyf-1::dyf-5b-gDNA and cloned into pDONR via In-Fusion Advantage PCR Cloning Kit
pDONR-Pdyf-1::adr-2	TGTAAGCTTGTC AAAATGTCCGTC GAAGAAGGTAT G	GAAGAGTAATT GGACTTAATTT ATAGTAAACAT TTG	<i>adr-2</i> genomic sequence was amplified from N2 and inserted into pDONR plasmid via In-Fusion Advantage PCR Cloning Kit.
pDONR-Pdyf-1::adr-2::gfp	TGTAAGCTTGTC AAAATGTCCGTC GAAGAAGGTAT G	ACCAAGCTTGG GTCTATTTATA GTAAACATTTG AA	<i>adr-2</i> genomic sequence was amplified from N2 and inserted into pDONR plasmid via In-Fusion Advantage PCR Cloning Kit.
pDONR-Pdyf-1::adbp-1::gfp	TGTAAGCTTGTC AAAATGAGCTTC GCCAGTGGATG	ACCGCTACCAC TTCCAGCACAA TTAACAATACT TGGAGC	<i>adbp-1</i> genomic sequence was amplified from N2 and inserted into pDONR plasmid via In-Fusion Advantage PCR Cloning Kit.
pDONR-Pdyf-1::nekl-4-gDNA	TGTAAGCTTGTC AAAATGACAGA GGAGGTTGGCCA	GAAGAGTAATT GGACTCACTTC GCTGCTGGATT TT	<i>nekl-4</i> genomic sequence was amplified from N2 and inserted into pDONR plasmid via In-Fusion Advantage PCR Cloning Kit.
pDONR-Pdyf-1::dyf-18-gDNA::wrmScarlet	TGTAAGCTTGTC AAAATGCCATCC TCTATTTATCGA	TTACTTGTAGA GCTCGTCCATT CC	<i>dyf-18</i> genomic sequence was amplified from N2 and inserted into pDONR plasmid via In-Fusion Advantage PCR Cloning Kit.

Table S4. Oligonucleotides for qPCR in this study

Name	Primers (For: forward)	Primers (Rev: reverse)
<i>act-5</i>	CGACATCAGAAAGGATCTCTAC	TCTTCATTGTGCTTGGAGCCAA
<i>dyf-5-E3E4</i>	TTGAGAGAGGTAATTCGTGAAA	TTTCGGGTTTCATATCTCGATG
<i>dyf-5-E9E10</i>	ATGCGTACGGTTACATCCCAA	GCCCAATCGACTCGACCC
<i>wrmScarlet</i>	GACATCAAGATGGCCCTCCGT	GCTCGTATTGCTCGACGACGG
<i>gfp</i>	TCCATGGCCAACACTTGTC	CTTCAGCACGTGTCTTGTAG

Table S5. Oligonucleotides for qPCR of RNA stability in this study

Name	Primers (For: forward)	Primers (Rev: reverse)
<i>act-5</i>	CAACATTCAGGCTGTGCTTTCCTT	GCGCTGTGAGCCTGTTTCTG
<i>dyf-5-E2</i>	CGCAGAAAAACGAATATTGCCAG	GTCTGGGCATTATTATCTGGATCC

References and Notes

1. P. Lahiry, A. Torkamani, N. J. Schork, R. A. Hegele, Kinase mutations in human disease: Interpreting genotype-phenotype relationships. *Nat. Rev. Genet.* **11**, 60–74 (2010). [doi:10.1038/nrg2707](https://doi.org/10.1038/nrg2707) [Medline](#)
2. J. Burghoorn, M. P. J. Dekkers, S. Rademakers, T. de Jong, R. Willemsen, G. Jansen, Mutation of the MAP kinase DYF-5 affects docking and undocking of kinesin-2 motors and reduces their speed in the cilia of *Caenorhabditis elegans*. *Proc. Natl. Acad. Sci. U.S.A.* **104**, 7157–7162 (2007). [doi:10.1073/pnas.0606974104](https://doi.org/10.1073/pnas.0606974104) [Medline](#)
3. N. Vasan, J. Baselga, D. M. Hyman, A view on drug resistance in cancer. *Nature* **575**, 299–309 (2019). [doi:10.1038/s41586-019-1730-1](https://doi.org/10.1038/s41586-019-1730-1) [Medline](#)
4. S. A. Berman, N. F. Wilson, N. A. Haas, P. A. Lefebvre, A novel MAP kinase regulates flagellar length in *Chlamydomonas*. *Curr. Biol.* **13**, 1145–1149 (2003). [doi:10.1016/S0960-9822\(03\)00415-9](https://doi.org/10.1016/S0960-9822(03)00415-9) [Medline](#)
5. Y. Omori, T. Chaya, K. Katoh, N. Kajimura, S. Sato, K. Muraoka, S. Ueno, T. Koyasu, M. Kondo, T. Furukawa, Negative regulation of ciliary length by ciliary male germ cell-associated kinase (Mak) is required for retinal photoreceptor survival. *Proc. Natl. Acad. Sci. U.S.A.* **107**, 22671–22676 (2010). [doi:10.1073/pnas.1009437108](https://doi.org/10.1073/pnas.1009437108) [Medline](#)
6. J. F. Reiter, M. R. Leroux, Genes and molecular pathways underpinning ciliopathies. *Nat. Rev. Mol. Cell Biol.* **18**, 533–547 (2017). [doi:10.1038/nrm.2017.60](https://doi.org/10.1038/nrm.2017.60) [Medline](#)
7. R. K. Ozgöl, A. M. Siemiatkowska, D. Yücel, C. A. Myers, R. W. Collin, M. N. Zonneveld, A. Beryozkin, E. Banin, C. B. Hoyng, L. I. van den Born, R. Bose, W. Shen, D. Sharon, F. P. Cremers, B. J. Klevering, A. I. den Hollander, J. C. Corbo; European Retinal Disease Consortium, Exome sequencing and cis-regulatory mapping identify mutations in MAK, a gene encoding a regulator of ciliary length, as a cause of retinitis pigmentosa. *Am. J. Hum. Genet.* **89**, 253–264 (2011). [doi:10.1016/j.ajhg.2011.07.005](https://doi.org/10.1016/j.ajhg.2011.07.005) [Medline](#)
8. B. A. Tucker, T. E. Scheetz, R. F. Mullins, A. P. DeLuca, J. M. Hoffmann, R. M. Johnston, S. G. Jacobson, V. C. Sheffield, E. M. Stone, Exome sequencing and analysis of induced pluripotent stem cells identify the cilia-related gene male germ cell-associated kinase (MAK) as a cause of retinitis pigmentosa. *Proc. Natl. Acad. Sci. U.S.A.* **108**, E569–E576 (2011). [doi:10.1073/pnas.1108918108](https://doi.org/10.1073/pnas.1108918108) [Medline](#)
9. P. D. Mace, Y. Wallez, M. F. Egger, M. K. Dobaczewska, H. Robinson, E. B. Pasquale, S. J. Riedl, Structure of ERK2 bound to PEA-15 reveals a mechanism for rapid release of activated MAPK. *Nat. Commun.* **4**, 1681 (2013). [doi:10.1038/ncomms2687](https://doi.org/10.1038/ncomms2687) [Medline](#)
10. Z. Fu, M. J. Schroeder, J. Shabanowitz, P. Kaldis, K. Togawa, A. K. Rustgi, D. F. Hunt, T. W. Sturgill, Activation of a nuclear Cdc2-related kinase within a mitogen-activated protein kinase-like TDY motif by autophosphorylation and cyclin-dependent protein kinase-activating kinase. *Mol. Cell. Biol.* **25**, 6047–6064 (2005). [doi:10.1128/MCB.25.14.6047-6064.2005](https://doi.org/10.1128/MCB.25.14.6047-6064.2005) [Medline](#)
11. L. A. Perkins, E. M. Hedgecock, J. N. Thomson, J. G. Culotti, Mutant sensory cilia in the nematode *Caenorhabditis elegans*. *Dev. Biol.* **117**, 456–487 (1986). [doi:10.1016/0012-1606\(86\)90314-3](https://doi.org/10.1016/0012-1606(86)90314-3) [Medline](#)

12. G. Ou, O. E. Blacque, J. J. Snow, M. R. Leroux, J. M. Scholey, Functional coordination of intraflagellar transport motors. *Nature* **436**, 583–587 (2005). [doi:10.1038/nature03818](https://doi.org/10.1038/nature03818) [Medline](#)
13. K. Nishikura, A-to-I editing of coding and non-coding RNAs by ADARs. *Nat. Rev. Mol. Cell Biol.* **17**, 83–96 (2016). [doi:10.1038/nrm.2015.4](https://doi.org/10.1038/nrm.2015.4) [Medline](#)
14. L. A. Tonkin, L. Saccomanno, D. P. Morse, T. Brodigan, M. Krause, B. L. Bass, RNA editing by ADARs is important for normal behavior in *Caenorhabditis elegans*. *EMBO J.* **21**, 6025–6035 (2002). [doi:10.1093/emboj/cdf607](https://doi.org/10.1093/emboj/cdf607) [Medline](#)
15. M. C. Washburn, B. Kakaradov, B. Sundararaman, E. Wheeler, S. Hoon, G. W. Yeo, H. A. Hundley, The dsRBP and inactive editor ADR-1 utilizes dsRNA binding to regulate A-to-I RNA editing across the *C. elegans* transcriptome. *Cell Rep.* **6**, 599–607 (2014). [doi:10.1016/j.celrep.2014.01.011](https://doi.org/10.1016/j.celrep.2014.01.011) [Medline](#)
16. J. A. Arribere, H. Kuroyanagi, H. A. Hundley, mRNA Editing, Processing and Quality Control in *Caenorhabditis elegans*. *Genetics* **215**, 531–568 (2020). [doi:10.1534/genetics.119.301807](https://doi.org/10.1534/genetics.119.301807) [Medline](#)
17. H. Q. Zhao, P. Zhang, H. Gao, X. He, Y. Dou, A. Y. Huang, X.-M. Liu, A. Y. Ye, M.-Q. Dong, L. Wei, Profiling the RNA editomes of wild-type *C. elegans* and ADAR mutants. *Genome Res.* **25**, 66–75 (2015). [doi:10.1101/gr.176107.114](https://doi.org/10.1101/gr.176107.114) [Medline](#)
18. H. Ohta, M. Fujiwara, Y. Ohshima, T. Ishihara, ADBP-1 regulates an ADAR RNA-editing enzyme to antagonize RNA-interference-mediated gene silencing in *Caenorhabditis elegans*. *Genetics* **180**, 785–796 (2008). [doi:10.1534/genetics.108.093310](https://doi.org/10.1534/genetics.108.093310) [Medline](#)
19. D. P. Reich, K. M. Tyc, B. L. Bass, *C. elegans* ADARs antagonize silencing of cellular dsRNAs by the antiviral RNAi pathway. *Genes Dev.* **32**, 271–282 (2018). [doi:10.1101/gad.310672.117](https://doi.org/10.1101/gad.310672.117) [Medline](#)
20. M. B. Warf, B. A. Shepherd, W. E. Johnson, B. L. Bass, Effects of ADARs on small RNA processing pathways in *C. elegans*. *Genome Res.* **22**, 1488–1498 (2012). [doi:10.1101/gr.134841.111](https://doi.org/10.1101/gr.134841.111) [Medline](#)
21. F. Zhang, Y. Lu, S. Yan, Q. Xing, W. Tian, SPRINT: An SNP-free toolkit for identifying RNA editing sites. *Bioinformatics* **33**, 3538–3548 (2017). [doi:10.1093/bioinformatics/btx473](https://doi.org/10.1093/bioinformatics/btx473) [Medline](#)
22. R. Middleton, D. Gao, A. Thomas, B. Singh, A. Au, J. J.-L. Wong, A. Bomane, B. Cosson, E. Eyraas, J. E. J. Rasko, W. Ritchie, IRFinder: Assessing the impact of intron retention on mammalian gene expression. *Genome Biol.* **18**, 51 (2017). [doi:10.1186/s13059-017-1184-4](https://doi.org/10.1186/s13059-017-1184-4) [Medline](#)
23. J. Rodriguez, J. S. Menet, M. Rosbash, Nascent-seq indicates widespread cotranscriptional RNA editing in *Drosophila*. *Mol. Cell* **47**, 27–37 (2012). [doi:10.1016/j.molcel.2012.05.002](https://doi.org/10.1016/j.molcel.2012.05.002) [Medline](#)
24. T. Kurosaki, M. W. Popp, L. E. Maquat, Quality and quantity control of gene expression by nonsense-mediated mRNA decay. *Nat. Rev. Mol. Cell Biol.* **20**, 406–420 (2019). [doi:10.1038/s41580-019-0126-2](https://doi.org/10.1038/s41580-019-0126-2) [Medline](#)

25. A. Grimson, S. O'Connor, C. L. Newman, P. Anderson, SMG-1 is a phosphatidylinositol kinase-related protein kinase required for nonsense-mediated mRNA Decay in *Caenorhabditis elegans*. *Mol. Cell. Biol.* **24**, 7483–7490 (2004). [doi:10.1128/MCB.24.17.7483-7490.2004](https://doi.org/10.1128/MCB.24.17.7483-7490.2004) [Medline](#)
26. L. Johns, A. Grimson, S. L. Kuchma, C. L. Newman, P. Anderson, *Caenorhabditis elegans* SMG-2 selectively marks mRNAs containing premature translation termination codons. *Mol. Cell. Biol.* **27**, 5630–5638 (2007). [doi:10.1128/MCB.00410-07](https://doi.org/10.1128/MCB.00410-07) [Medline](#)
27. F. Usuki, A. Yamashita, T. Shiraishi, A. Shiga, O. Onodera, I. Higuchi, S. Ohno, Inhibition of SMG-8, a subunit of SMG-1 kinase, ameliorates nonsense-mediated mRNA decay-exacerbated mutant phenotypes without cytotoxicity. *Proc. Natl. Acad. Sci. U.S.A.* **110**, 15037–15042 (2013). [doi:10.1073/pnas.1300654110](https://doi.org/10.1073/pnas.1300654110) [Medline](#)
28. R. R. Chivukula, D. T. Montoro, H. M. Leung, J. Yang, H. E. Shamseldin, M. S. Taylor, G. W. Dougherty, M. A. Zariwala, J. Carson, M. L. A. Daniels, P. R. Sears, K. E. Black, L. P. Hariri, I. Almogarrri, E. M. Frenkel, V. Vinarsky, H. Omran, M. R. Knowles, G. J. Tearney, F. S. Alkuraya, D. M. Sabatini, A human ciliopathy reveals essential functions for NEK10 in airway mucociliary clearance. *Nat. Med.* **26**, 244–251 (2020). [doi:10.1038/s41591-019-0730-x](https://doi.org/10.1038/s41591-019-0730-x) [Medline](#)
29. A. K. Maurya, T. Rogers, P. Sengupta, A CCRK and a MAK Kinase Modulate Cilia Branching and Length via Regulation of Axonemal Microtubule Dynamics in *Caenorhabditis elegans*. *Curr. Biol.* **29**, 1286–1300.e4 (2019). [doi:10.1016/j.cub.2019.02.062](https://doi.org/10.1016/j.cub.2019.02.062) [Medline](#)
30. K. M. Power, J. S. Akella, A. Gu, J. D. Walsh, S. Bellotti, M. Morash, W. Zhang, Y. H. Ramadan, N. Ross, A. Golden, H. E. Smith, M. M. Barr, R. O'Hagan, Mutation of NEKL-4/NEK10 and TTLL genes suppress neuronal ciliary degeneration caused by loss of CCPP-1 deglutamylase function. *PLOS Genet.* **16**, e1009052 (2020). [doi:10.1371/journal.pgen.1009052](https://doi.org/10.1371/journal.pgen.1009052) [Medline](#)
31. S. H. Schmidt, M. J. Knape, D. Boassa, N. Mumdey, A. P. Kornev, M. H. Ellisman, S. S. Taylor, F. W. Herberg, The dynamic switch mechanism that leads to activation of LRRK2 is embedded in the DFG ψ motif in the kinase domain. *Proc. Natl. Acad. Sci. U.S.A.* **116**, 14979–14988 (2019). [doi:10.1073/pnas.1900289116](https://doi.org/10.1073/pnas.1900289116) [Medline](#)
32. L. Xia, D. Robinson, A.-H. Ma, H.-C. Chen, F. Wu, Y. Qiu, H.-J. Kung, Identification of human male germ cell-associated kinase, a kinase transcriptionally activated by androgen in prostate cancer cells. *J. Biol. Chem.* **277**, 35422–35433 (2002). [doi:10.1074/jbc.M203940200](https://doi.org/10.1074/jbc.M203940200) [Medline](#)
33. S. W. Knight, B. L. Bass, The role of RNA editing by ADARs in RNAi. *Mol. Cell* **10**, 809–817 (2002). [doi:10.1016/S1097-2765\(02\)00649-4](https://doi.org/10.1016/S1097-2765(02)00649-4) [Medline](#)
34. H. Tabara, E. Yigit, H. Siomi, C. C. Mello, The dsRNA binding protein RDE-4 interacts with RDE-1, DCR-1, and a DExH-box helicase to direct RNAi in *C. elegans*. *Cell* **109**, 861–871 (2002). [doi:10.1016/S0092-8674\(02\)00793-6](https://doi.org/10.1016/S0092-8674(02)00793-6) [Medline](#)
35. V. Pelechano, L. M. Steinmetz, Gene regulation by antisense transcription. *Nat. Rev. Genet.* **14**, 880–893 (2013). [doi:10.1038/nrg3594](https://doi.org/10.1038/nrg3594) [Medline](#)

36. A. J. Albee, A. L. Kwan, H. Lin, D. Granas, G. D. Stormo, S. K. Dutcher, Identification of cilia genes that affect cell-cycle progression using whole-genome transcriptome analysis in *Chlamydomonas reinhardtii*. *G3* **3**, 979–991 (2013). [doi:10.1534/g3.113.006338](https://doi.org/10.1534/g3.113.006338) [Medline](#)
37. P. Walter, D. Ron, The unfolded protein response: From stress pathway to homeostatic regulation. *Science* **334**, 1081–1086 (2011). [doi:10.1126/science.1209038](https://doi.org/10.1126/science.1209038) [Medline](#)
38. C. Calabrese, N. R. Davidson, D. Demircioğlu, N. A. Fonseca, Y. He, A. Kahles, K.-V. Lehmann, F. Liu, Y. Shiraishi, C. M. Soulette, L. Urban, L. Greger, S. Li, D. Liu, M. D. Perry, Q. Xiang, F. Zhang, J. Zhang, P. Bailey, S. Erkek, K. A. Hoadley, Y. Hou, M. R. Huska, H. Kilpinen, J. O. Korbil, M. G. Marin, J. Markowski, T. Nandi, Q. Pan-Hammarström, C. S. Pedamallu, R. Siebert, S. G. Stark, H. Su, P. Tan, S. M. Waszak, C. Yung, S. Zhu, P. Awadalla, C. J. Creighton, M. Meyerson, B. F. F. Ouellette, K. Wu, H. Yang, A. Brazma, A. N. Brooks, J. Göke, G. Rätsch, R. F. Schwarz, O. Stegle, Z. Zhang; PCAWG Transcriptome Core Group; PCAWG Transcriptome Working Group; PCAWG Consortium, Genomic basis for RNA alterations in cancer. *Nature* **578**, 129–136 (2020). [doi:10.1038/s41586-020-1970-0](https://doi.org/10.1038/s41586-020-1970-0) [Medline](#)
39. H. Chung, J. J. A. Calis, X. Wu, T. Sun, Y. Yu, S. L. Sarbanes, V. L. Dao Thi, A. R. Shilvock, H.-H. Hoffmann, B. R. Rosenberg, C. M. Rice, Human ADAR1 Prevents Endogenous RNA from Triggering Translational Shutdown. *Cell* **172**, 811–824.e14 (2018). [doi:10.1016/j.cell.2017.12.038](https://doi.org/10.1016/j.cell.2017.12.038) [Medline](#)
40. J. J. Ishizuka, R. T. Manguso, C. K. Cheruiyot, K. Bi, A. Panda, A. Iracheta-Vellve, B. C. Miller, P. P. Du, K. B. Yates, J. Dubrot, I. Buchumenski, D. E. Comstock, F. D. Brown, A. Ayer, I. C. Kohnle, H. W. Pope, M. D. Zimmer, D. R. Sen, S. K. Lane-Reticker, E. J. Robitschek, G. K. Griffin, N. B. Collins, A. H. Long, J. G. Doench, D. Kozono, E. Y. Levanon, W. N. Haining, Loss of ADAR1 in tumours overcomes resistance to immune checkpoint blockade. *Nature* **565**, 43–48 (2019). [doi:10.1038/s41586-018-0768-9](https://doi.org/10.1038/s41586-018-0768-9) [Medline](#)
41. S. Brenner, The genetics of *Caenorhabditis elegans*. *Genetics* **77**, 71–94 (1974). [doi:10.1093/genetics/77.1.71](https://doi.org/10.1093/genetics/77.1.71) [Medline](#)
42. D. J. Dickinson, J. D. Ward, D. J. Reiner, B. Goldstein, Engineering the *Caenorhabditis elegans* genome using Cas9-triggered homologous recombination. *Nat. Methods* **10**, 1028–1034 (2013). [doi:10.1038/nmeth.2641](https://doi.org/10.1038/nmeth.2641) [Medline](#)
43. A. E. Friedland, Y. B. Tzur, K. M. Esvelt, M. P. Colaiácovo, G. M. Church, J. A. Calarco, Heritable genome editing in *C. elegans* via a CRISPR-Cas9 system. *Nat. Methods* **10**, 741–743 (2013). [doi:10.1038/nmeth.2532](https://doi.org/10.1038/nmeth.2532) [Medline](#)
44. E. M. Hedgecock, J. G. Culotti, J. N. Thomson, L. A. Perkins, Axonal guidance mutants of *Caenorhabditis elegans* identified by filling sensory neurons with fluorescein dyes. *Dev. Biol.* **111**, 158–170 (1985). [doi:10.1016/0012-1606\(85\)90443-9](https://doi.org/10.1016/0012-1606(85)90443-9) [Medline](#)
45. T. A. Starich, R. K. Herman, C. K. Kari, W. H. Yeh, W. S. Schackwitz, M. W. Schuyler, J. Collet, J. H. Thomas, D. L. Riddle, Mutations affecting the chemosensory neurons of *Caenorhabditis elegans*. *Genetics* **139**, 171–188 (1995). [doi:10.1093/genetics/139.1.171](https://doi.org/10.1093/genetics/139.1.171) [Medline](#)

46. P. N. Inglis, G. Ou, M. R. Leroux, J. M. Scholey, The sensory cilia of *Caenorhabditis elegans*. *WormBook* 1–22 (2007). [doi:10.1895/wormbook.1.126.2](https://doi.org/10.1895/wormbook.1.126.2) [Medline](#)
47. A. Mukhopadhyay, B. Deplancke, A. J. Walhout, H. A. Tissenbaum, Chromatin immunoprecipitation (ChIP) coupled to detection by quantitative real-time PCR to study transcription factor binding to DNA in *Caenorhabditis elegans*. *Nat. Protoc.* **3**, 698–709 (2008). [doi:10.1038/nprot.2008.38](https://doi.org/10.1038/nprot.2008.38) [Medline](#)

RNA editing restricts hyperactive ciliary kinases

Dongdong Li, Yufan Liu, Peishan Yi, Zhiwen Zhu, Wei Li, Qiangfeng Cliff Zhang, Jin Billy Li and Guangshuo Ou

Science **373** (6558), 984-991.
DOI: 10.1126/science.abd8971

RNA editing restricts ciliary kinases

Ciliary kinases are essential for cilia formation and function but it remains unknown how their activities are regulated *in vivo*. Li *et al.* created roundworm animal models carrying hyperactive ciliary kinases that disrupt cilia. Their genetic suppressor screens revealed that loss of an RNA adenosine deaminase that catalyzes adenosine-to-inosine (A-to-I) RNA editing rescued ciliary abnormalities. They found that kinase hyperactivation caused this RNA adenosine deaminase to edit kinase RNA and impair kinase RNA splicing and translation, thereby downregulating ciliary kinases from nuclei. These results suggest that ciliopathies may be treated by targeting the pathways outside of cilia.

Science, abd8971, this issue p. 984

ARTICLE TOOLS

<http://science.sciencemag.org/content/373/6558/984>

SUPPLEMENTARY MATERIALS

<http://science.sciencemag.org/content/suppl/2021/08/25/373.6558.984.DC1>

REFERENCES

This article cites 47 articles, 19 of which you can access for free
<http://science.sciencemag.org/content/373/6558/984#BIBL>

PERMISSIONS

<http://www.sciencemag.org/help/reprints-and-permissions>

Use of this article is subject to the [Terms of Service](#)

Science (print ISSN 0036-8075; online ISSN 1095-9203) is published by the American Association for the Advancement of Science, 1200 New York Avenue NW, Washington, DC 20005. The title *Science* is a registered trademark of AAAS.

Copyright © 2021 The Authors, some rights reserved; exclusive licensee American Association for the Advancement of Science. No claim to original U.S. Government Works